JOURNAL OF GLACIOLOGY

CAMBRIDGE UNIVERSITY PRESS

Vulnerability of Firn to Hydrofracture: Poromechanics Modeling

Journal:	*Journal of Glaciology*
Manuscript ID	JOG-23-0036
Manuscript Type:	Article
Date Submitted by the Author:	13-Mar-2023
Complete List of Authors:	Meng, Yue; Princeton University, Department of Geosciences Culberg , Riley ; Princeton University, Geosciences Lai, Ching-Yao; Princeton University, Department of Geosciences
Keywords:	Polar firn, Glacier hydrology, Glacier mechanics, Ice-sheet mass balance
Abstract:	On the Greenland Ice Sheet, hydrofracture connects the supraglacial and subglacial hydrologic systems, coupling surface runoff dynamics and ice velocity. Over the last two decades, the growth of low-permeability ice slabs in the firn above the equilibrium line has expanded Greenland’s runoff zone, but the vulnerability of these regions to hydrofracture is still poorly understood. Observations from Northwest Greenland suggest that when meltwater drains through crevasses in ice slabs, it is stored in the underlying relict firn layer and does not reach the ice sheet bed. Here, we use poromechanics to investigate whether water-filled crevasses in ice slabs can propagate vertically through a firn layer. Based on numerical simulations, we develop an analytical estimate of the water injection-induced effective stress in the firn given the water level in the

	crevasse, ice slab thickness, and firn properties. We find that the firn layer reduces the system's vulnerability to hydrofracture because much of the hydrostatic stress is accommodated by a change in pore pressure, rather than being transmitted to the solid skeleton. This result suggests that surface-to-bed hydrofracture will not occur in ice slab regions until all pore space proximal to the initial flaw has been filled with solid ice.

CAMBRIDGE UNIVERSITY PRESS

Article-type

Keywords:
Greenland, firn, ice slabs, hydrofracture, poromechanics

Author for correspondence:
Yue Meng, Riley Culberg,
E-mail: om3193@princeton.edu,
rtculberg@princeton.edu

Vulnerability of Firn to Hydrofracture: Poromechanics Modeling

Yue Meng*, Riley Culberg*, and Ching-Yao Lai

Department of Geosciences, Princeton University, Princeton, NJ, USA

Abstract

On the Greenland Ice Sheet, hydrofracture connects the supraglacial and subglacial hydrologic systems, coupling surface runoff dynamics and ice velocity. Over the last two decades, the growth of low-permeability ice slabs in the firn above the equilibrium line has expanded Greenland's runoff zone, but the vulnerability of these regions to hydrofracture is still poorly understood. Observations from Northwest Greenland suggest that when meltwater drains through crevasses in ice slabs, it is stored in the underlying relict firn layer and does not reach the ice sheet bed. Here, we use poromechanics to investigate whether water-filled crevasses in ice slabs can propagate vertically through a firn layer. Based on numerical simulations, we develop an analytical estimate of the water injection-induced effective stress in the firn given the water level in the crevasse, ice slab thickness, and firn properties. We find that the firn layer reduces the system's vulnerability to hydrofracture because much of the hydrostatic stress is accommodated by a change in pore pressure, rather than being transmitted to the solid skeleton. This result suggests that surface-to-bed hydrofracture will not occur in ice slab regions until all pore space proximal to the initial flaw has been filled with solid ice.

1. Introduction

Over the last two decades, around 55% of mass loss from the Greenland Ice Sheet has come from the runoff of surface meltwater, with the remainder driven by ice dynamics (Mouginot and others, 2019; Van Den Broeke and others, 2009). Passive microwave observations and regional climate models also show a long-term increase in the area of the ice sheet experience surface melt, the upper elevation of melting, and the total length of the annual melt season (Colosio and others, 2021; Fettweis and others, 2011). Therefore, understanding how much and how quickly surface meltwater can be transported through the supraglacial and englacial hydrologic systems and how those systems are evolving with time is critical for assessing current and future sea level contributions from the Greenland Ice Sheet.

Water transport processes vary significantly across the ice sheet. In the bare ice ablation zone, surface meltwater flows efficiently over the impermeable ice surface in streams or river and forms lakes in closed basins (Smith and others, 2015; Yang and Smith, 2016). Particularly in Southwest Greenland, this supraglacial system is connected to the ice sheet bed through fractures, moulins, and rapid lake drainage events and most melt eventually enters the subglacial system (Das and others, 2008; Koziol and others, 2017; Poinar and Andrews, 2021; Andrews and others, 2018; Hoffman and others, 2018; Dow and others, 2015; Lai and others, 2021). These englacial transport pathways are primarily formed by hydrofracture (Stevens and others, 2015; Poinar and others, 2017) and lead to a coupling between surface melting and ice dynamics, where meltwater delivery to the bed can cause transient, seasonal increases in ice velocity that may temporarily increase ice discharge (Moon and others, 2014; Schoof, 2010; Zwally and others, 2002).

In contrast, in the accumulation zone, meltwater percolates in the porous near-surface firn layer, where it may refreeze locally (Harper and others, 2012; Machguth and others, 2016) or be stored in buried liquid water aquifers (Forster and others, 2014). These processes buffer runoff and prevent water from reaching the subglacial system as long a spore space remains for storage. The processes by which the percolation zone may transition to a bare ice ablation zone under persistent atmospheric warming are not yet fully understood, particularly the timescales over which the hydrologic system evolves from local retention to efficient runoff.

The development of multi-meter thick ice slabs in the near-surface firn of the wet snow zone appears to be a mechanism by which the ice sheet may transition rapidly from retention to runoff. These continuous, low-permeability layers of refrozen ice block vertical percolation and allow water flow freely over the surface, despite the presence of a relict porous firn layer at depth (MacFerrin and others, 2019; Tedstone and Machguth, 2022). This produces a surface hydrologic network that qualitatively resembles that of the bare ice ablation zone (Tedstone and Machguth, 2022; Yang and Smith, 2016). However, it remains unclear whether surface-to-bed connections form via hydrofracture in ice slab regions and therefore, whether ice slab formation is a direct precursor to meltwater forcing of the subglacial system at these higher elevations. Poinar and others (2015) argued that, in Southwest Greenland, surface strain rates were insufficient for hydrofracture and runoff would largely flow downstream over the surface to the ablation zone. However, other studies of the same areas found no evidence of an elevation limit on hydrofracture (Christoffersen and others, 2018; Yang and Smith, 2016).

Culberg and others (2022) investigated the hydrology of the Northwest Greenland ice slab area and showed that while surface meltwater does drain into fractures in the ice slabs, it appears to largely be stored in the underlying porous firn layer, rather than reaching the bed. These saturated firn layers refreeze over time to form massive buried ice complexes known as "ice blobs" (Culberg and others, 2022). However, the authors also note evidence for the drainage of persistent buried supraglacial lakes in this same region (Culberg and others, 2022). In fact, basins where an ice blob has formed may later develop supraglacial lakes that then drain to the ice sheet bed (see example in Figure 1). These observations lead to two important questions.

1. Why do vertical fractures in ice slabs not propagate unstably when filled with water?
2. What drives the transition to full ice thickness hydrofracture once all pore space directly beneath a lake has been filled by refreezing?

Current models of ice sheet hydrofracture are poorly suited to address these questions. The most common approach is to use linear elastic fracture mechanics (LEFM). Two underlying assumptions of this approach as implemented in the glaciological literature are that ice is incompressible and impermeable (Lai and others, 2020; Van Der Veen, 1998; van der Veen, 2007). Existing models have not considered a porous, compacting firn layer beneath an impermeable ice slab, making it difficult to address the impact of firn on fracture propagation. Lai and others (2020) have treated the effects of a near-surface firn layer on dry fracture propagation. They assumed that due to its lower density, the presence of firn leads to a lower overburden stress, lower fracture toughness, and reduced viscosity, neglecting leakage of water into the firn (Lai and others, 2020). However, work in other fields on the hydraulic fracturing of permeable reservoir suggests that for water-filled fractures in a porous medium, leak-off of fluid into the surrounding material can significantly alter the fracture propagation (Bunger and others, 2005; Chen and others, 2021; Detournay, 2016; Meng and others, 2020, 2022).

Here, we a develop a poromechanical model to predict the effective stress in the firn layer beneath a water-filled fracture in an ice slab. This approach can describe both fluid flow out of the fracture and the solid-fluid coupling that impacts stress. Based on these simulations, we propose an analytical model for the maximum effective stress in the firn layer for both constant water pressure and constant injection rate conditions. We then apply this model to assess the vulnerability of Greenland's ice slab regions to hydrofracture and analyze the behavior of the system as a function of water availability, ice slab thickness, and the mechanical and hydraulic properties of the firn.

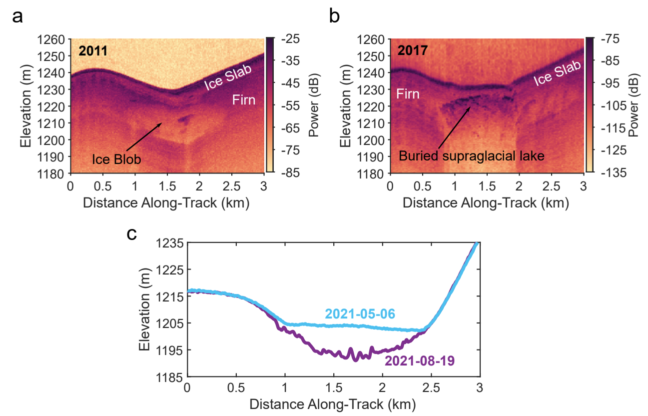

Fig. 1. Ice-penetrating radar observations of firn water storage in Northwest Greenland. a) Radar observations in 2011 show an ice blob that had refrozen in the porous firn beneath the ice slab. b) By 2017, a buried supraglacial lake formed on the surface overtop the ice blob. c) This buried supraglacial lake drained to the ice sheet bed between May and August 2021. The change in surface elevation is shown here along a transect extracted from ArcticDEM data collected before and after the drainage.

2. Methods

In regions with high velocity gradients, dry surface fractures may form in ice slabs. If meltwater flows into these crevasses, they may continue to propagate until they reach the underneath permeable firn layer (Figure 2). The meltwater then penetrates into the firn layer either by infiltration or fracturing. Previous research has used two-phase continuum models to study meltwater flow through snow without considering flow-induced deformation in the porous snow layer (Meyer and Hewitt, 2017; Moure and others, 2022). We develop a two-dimensional, poroelastic continuum model to quantify the stress and pressure changes in the firn layer during meltwater penetration (Biot, 1941; Wang, 2000; Coussy, 2004). Here, we consider two scenarios of water infiltration into the porous firn layer:

1. Constant pressure boundary condition : a constant water height (H_w) in the surface crevasse.
2. Constant flow rate boundary condition: a constant water injection velocity (V_{inj}) at the crevasse tip.

When stress is applied to porous media, part of the stress is transmitted through the pore fluid and part of the stress is transmitted through the solid skeleton. Effective stress (σ')—the fraction of the total stress (σ) that is transmitted through the solid skeleton—controls the mechanical behavior of porous media (Terzaghi, 1925, 1943). To rationalize the crossover from infiltration to fracturing regimes quantitatively, we adopt a fracturing criterion for the cohesive porous firn layer: the horizontal tensile effective stress (σ'_{xx}) should exceed the material tensile strength (σ'_t) to generate vertical fractures (Engelder and others, 1990).

2.1 Initial stresses before water infiltration

We assume the porous firn layer to be an isotropic, linear elastic continuum. Figure 2 shows the stresses acting on the firn layer from lithostatic stresses and water hydrostatic pressure. As the lateral extents in x and y directions ($2 \sim 10$ km) are much larger than in the z direction ($30 \sim 50$ m), we intially assume uniaxial strain conditions with $\epsilon_{xx} = \epsilon_{yy} = 0$, which is a common assumption for geomechanics or hydrology (Wang, 2000).

Following Coussy (2004), the poroelasticity equation states that

$$\delta\boldsymbol{\sigma} = \delta\boldsymbol{\sigma}' - b\delta p\boldsymbol{I}, \tag{1}$$

where $\boldsymbol{\sigma}$, $\boldsymbol{\sigma}'$, p are the Cauchy total stress tensor, the effective stress tensor, and the pore pressure, respectively, and $b \in [0, 1]$ is the Biot coefficient of the porous medium. Terzaghi's effective stress tensor $\boldsymbol{\sigma}'$ is the portion of the stress supported through deformation of the solid skeleton, and here we adopt the convention of tension being positive. The stress–strain constitutive equation for the linear elastic firn layer is:

$$\delta\boldsymbol{\sigma}' = \frac{3K\nu}{1+\nu}\epsilon_{kk}\boldsymbol{I} + \frac{3K(1-2\nu)}{1+\nu}\boldsymbol{\epsilon}, \tag{2}$$

where K, ν, $\boldsymbol{\epsilon}$ are the drained bulk modulus, the drained Poisson ratio of the firn layer (Biot, 1941; Terzaghi, 1943), and the strain tensor, respectively. The constitutive equations for uniaxial strain are obtained by inserting the constraint that $\epsilon_{xx} = \epsilon_{yy} = 0$ into Eqn. (1)-(2) and noting that $\epsilon_{kk} = \epsilon_{zz}$:

$$\delta\sigma_{xx}|_{\epsilon_{xx}=\epsilon_{yy}=0} = \delta\sigma_{yy}|_{\epsilon_{xx}=\epsilon_{yy}=0} = \frac{3K\nu}{1+\nu}\epsilon_{zz} - b\delta p, \tag{3}$$

$$\delta\sigma_{zz}|_{\epsilon_{xx}=\epsilon_{yy}=0} = \frac{3K(1-\nu)}{1+\nu}\epsilon_{zz} - b\delta p, \tag{4}$$

Solving Eqn. (4) for ϵ_{zz} and substituting into Eqn. (3) yields

$$\delta\sigma_{xx}|_{\epsilon_{xx}=\epsilon_{yy}=0} = \delta\sigma_{yy}|_{\epsilon_{xx}=\epsilon_{yy}=0} = \frac{\nu}{1-\nu}\delta\sigma_{zz} - \frac{1-2\nu}{1-\nu}b\delta p, \tag{5}$$

Before water penetrating into the surface crevasses, the firn layer is under initial lithostatic stresses only ($p = 0$). Effective stress equal total stress without the presence of pore pressure. Eqn. (5) gives the initial effective lateral stresses at the crevasse tip (point A in Figure 2):

$$\sigma_{xx,0}|_{p=0} = \sigma_{yy,0}|_{p=0} = \sigma'_{xx,0} = \sigma'_{yy,0} = \frac{\nu}{1-\nu}\sigma'_{zz} = -\frac{\nu}{1-\nu}\rho_i g H_i, \tag{6}$$

where ρ_i, H_i are the density and height of the ice slab above the firn layer, respectively. Therefore, the initial effective stresses for the porous firn layer are compressive under lithostatic conditions.

2.2 Water infiltration into the porous firn layer

Water injection into the firn induces a tensile effective stress change at the crevasse tip ($\delta\sigma'_{xx}$). When the horizontal effective stress exceeds the firn tensile strength, vertical fractures are generated (Engelder and others, 1990; Wang, 2000). The fracture criterion is written as follows:

$$\sigma'_{xx} = \sigma'_{xx,0} + \delta\sigma'_{xx} \geq \sigma'_t. \tag{7}$$

Figure 2 shows the stresses acting on the firn layer with water injection through a crevasse with opening ($2L_{\mathrm{crev}}$) with either a constant water height (H_w) or constant water injection velocity (V_{inj}). To quantify the stresses and pressure changes during the water infiltration into the dry cohesive firn layer, we develop a two-dimensional, two-phase poroelastic continuum model. In the following, we present the extension of Biot's theory (Jha and Juanes, 2014; Bjørnarå and others, 2016) to two-phase flow, where we consider small deformations. We assume plane-strain condition for this 2D model ($\epsilon_{yy} = 0$, $\frac{\partial}{\partial y} = 0$).

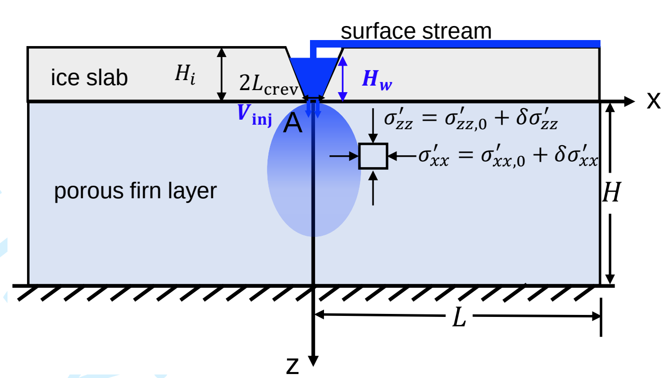

Fig. 2. A schematic showing stresses acting on the porous firn layer with water infiltration from the crevasse.

2.2.1 Geomechanical Equations

Under quasi-static conditions, the balance of linear momentum of the solid-fluid system states that:

$$\nabla \cdot \boldsymbol{\sigma} + \rho_b \boldsymbol{g} = \boldsymbol{0}, \tag{8}$$

where $\boldsymbol{g}$ is gravitational acceleration. The bulk density for the solid-fluid system is defined as $\rho_b \equiv (1-\phi)\rho_s + \phi\sum_\alpha \rho_\alpha S_\alpha$, where ρ_s is the solid ice density, ϕ is the porosity, and ρ_α and $S_\alpha \in [0, 1]$ are the density and saturation of the fluid phase α (water w or air a), respectively. The 2D stress balance equation becomes:

$$\begin{aligned} \frac{\partial\sigma_{xx}}{\partial x} + \frac{\partial\sigma_{zx}}{\partial z} &= 0, \quad \text{in x direction,} \\ \frac{\partial\sigma_{xz}}{\partial x} + \frac{\partial\sigma_{zz}}{\partial z} + \rho_b g &= 0, \quad \text{in z direction.} \end{aligned} \tag{9}$$

The strain tensor is defined as $\boldsymbol{\epsilon} = \frac{1}{2}[\nabla\boldsymbol{u} + (\nabla\boldsymbol{u})^T]$, where $\boldsymbol{u} = [u, y, w]$ is the displacement vector, and u, y, w are the displacements in x, y, z directions, respectively. For 2D deformation in plane-strain condition, the strains are written as:

$$\epsilon_{xx} = \frac{\partial u}{\partial x}, \quad \epsilon_{zz} = \frac{\partial w}{\partial z}, \quad \epsilon_{xz} = \frac{1}{2}\left(\frac{\partial u}{\partial z} + \frac{\partial w}{\partial x}\right), \quad \epsilon_{kk} = \epsilon_{xx} + \epsilon_{zz}. \tag{10}$$

Using equations (1), (2), (6) and (10), the stress balance equation (9) can be expressed as a function of displacements $u(x, z, t)$, $w(x, z, t)$, and pore pressure $p(x, z, t)$.

2.2.2 Fluid Flow Equations

For the two-phase immiscible flow system, the conservation of fluid mass can be written as follows:

$$\frac{\partial(\phi\rho_\alpha S_\alpha)}{\partial t} + \nabla \cdot (\rho_\alpha \phi S_\alpha \boldsymbol{v}_\alpha) = 0, \tag{11}$$

The phase velocity $\boldsymbol{v}_\alpha$ is related to the Darcy flux $\boldsymbol{q}_\alpha$ in a deforming medium by the following relation:

$$\boldsymbol{q}_\alpha = \phi S_\alpha(\boldsymbol{v}_\alpha - \boldsymbol{v}_s) = -\frac{k_0}{\eta_\alpha} k_{r\alpha}(\nabla p_\alpha - \rho_\alpha \boldsymbol{g}) \tag{12}$$

where $\boldsymbol{v}_s$ is the velocity of the solid skeleton, k_0 is the intrinsic permeability of the porous firn layer, $\boldsymbol{g}$ is the gravity vector, and η_α, $k_{r\alpha} = k_{r\alpha}(S_\alpha)$ and p_α are the dynamic viscosity, relative permeability, and fluid pressure for phase α (water w or air a), respectively. Since capillary pressure is negligible here, $p_c = p_w - p_a = 0$, the two phases have the same fluid pressure p. The relative permeability functions are given as Corey-type power law functions (Brooks, 1965; Meyer and Hewitt, 2017; Moure and others, 2022):

$$k_{rw} = S_w^a \quad \text{and} \quad k_{ra} = (1 - S_w)^b, \tag{13}$$

where the fitting parameters are the exponents $a = 3$ and $b = 2$ (Bjørnarå and others, 2016).

Considering the mass conservation of the solid phase:

$$\frac{\partial[\rho_s(1-\phi)]}{\partial t} + \nabla \cdot [\rho_s(1-\phi)\boldsymbol{v}_s] = 0 \tag{14}$$

Assuming isothermal conditions and using the equation of state for the solid, the following expression for the change in porosity is obtained (Lewis and Schrefler, 1998):

$$\frac{d\phi}{dt} = (b - \phi)\left(c_s \frac{dp}{dt} + \nabla \cdot \boldsymbol{v}_s\right) \tag{15}$$

where c_s is the compressibility of the solid phase. We use equations (12), (14), and (15) to expand equation (11) as follows:

$$\phi \frac{\partial S_\alpha}{\partial t} + S_\alpha \left(b \frac{\partial \epsilon_{kk}}{\partial t} + \frac{1}{M}\frac{\partial p}{\partial t}\right) + \nabla \cdot \boldsymbol{q}_\alpha = 0, \tag{16}$$

where ϵ_{kk} is the volumetric strain of the solid phase. The Biot modulus of the porous firn, M, is related to fluid and firn properties as $\frac{1}{M} = \phi S_w c_w + \phi(1 - S_w)c_a + (b - \phi)c_s$, where c_w, c_a are the water and air compressibility, respectively (Coussy, 2004). Adding equation (16) for water and air phases, and imposing that $S_a + S_w \equiv 1$ for the porous firn layer, we obtain the pressure diffusion equation:

$$b\frac{\partial \epsilon_{kk}}{\partial t} + \frac{1}{M}\frac{\partial p}{\partial t} + \nabla \cdot \boldsymbol{q}_t = 0, \tag{17}$$

where $\boldsymbol{q}_t = \boldsymbol{q}_w + \boldsymbol{q}_a$ is the total Darcy flux for water and air phases.

2.2.3 Summary of Governing Equations

We use a 2D, two-phase poroelastic continuum model to solve the infiltration-induced stress and pressure changes. The model has four governing equations, two derived from conservation of fluid mass [Eqn. (17) for the water–air fluid mixture and Eqn. (16) for the water phase] and two derived from conservation of linear momentum [Eqn. (9)]. The model solves the time evolution of four unknowns: (1) pore pressure field $p(x, z, t)$; (2) water saturation field $S_w(x, z, t)$; (3) horizontal displacement field $u(x, z, t)$, and (4) vertical displacement field $w(x, z, t)$ of the porous firn layer. The governing equations are summarized and written in x, z coordinates as follows:

$$\begin{aligned} &b\frac{\partial \epsilon_{kk}}{\partial t} + \frac{1}{M}\frac{\partial p}{\partial t} - k_0\frac{\partial}{\partial x}\left(\left(\frac{k_{rw}}{\eta_w} + \frac{k_{ra}}{\eta_a}\right)\frac{\partial p}{\partial x}\right) \\ &-k_0\frac{\partial}{\partial z}\left(\left(\frac{k_{rw}}{\eta_w} + \frac{k_{ra}}{\eta_a}\right)\frac{\partial p}{\partial z} - \left(\frac{\rho_w k_{rw}}{\eta_w} + \frac{\rho_a k_{ra}}{\eta_a}\right)g\right) = 0, \end{aligned} \tag{18}$$

$$\begin{aligned} \phi\frac{\partial S_w}{\partial t} + S_w\left(b\frac{\partial \epsilon_{kk}}{\partial t} + \frac{1}{M}\frac{\partial p}{\partial t}\right) - \frac{k_0}{\eta_w}\frac{\partial}{\partial x}\left(k_{rw}\frac{\partial p}{\partial x}\right) \\ -\frac{k_0}{\eta_w}\frac{\partial}{\partial z}\left(k_{rw}\left(\frac{\partial p}{\partial z} - \rho_w g\right)\right) = 0, \end{aligned} \tag{19}$$

$$\frac{\partial \sigma_{xx}}{\partial x} + \frac{\partial \sigma_{zx}}{\partial z} = 0, \tag{20}$$

$$\frac{\partial \sigma_{xz}}{\partial x} + \frac{\partial \sigma_{zz}}{\partial z} + \rho_b g = 0. \tag{21}$$

We denote the initial lithostatic stress condition as $\boldsymbol{\sigma_0}$. And we denote the fluid-induced stress and pressure changes as $\delta\boldsymbol{\sigma}$, δp. The total stresses are written in x, z coordinates as:

$$\sigma_{xx} = \sigma_{xx,0} + \delta\sigma_{xx}, \tag{22}$$

$$\sigma_{xz} = \sigma_{zx} = \delta\sigma_{xz} = \delta\sigma_{zx}, \tag{23}$$

$$\sigma_{zz} = \sigma_{zz,0} + \delta\sigma_{zz}, \tag{24}$$

Combining equations (1), (2), and (10), the two-phase poroelastic model calculates the infiltration-induced stresses and strains as:

$$\delta\sigma_{xx} = \frac{3K\nu}{1+\nu}\epsilon_{kk} + \frac{3K(1-2\nu)}{1+\nu}\epsilon_{xx} - b\delta p, \tag{25}$$

$$\delta\sigma_{xz} = \delta\sigma_{zx} = \frac{3K(1-2\nu)}{1+\nu}\epsilon_{xz}, \tag{26}$$

$$\delta\sigma_{zz} = \frac{3K\nu}{1+\nu}\epsilon_{kk} + \frac{3K(1-2\nu)}{1+\nu}\epsilon_{zz} - b\delta p, \tag{27}$$

$$\epsilon_{xx} = \frac{\partial u}{\partial x}, \quad \epsilon_{zz} = \frac{\partial w}{\partial z}, \quad \epsilon_{xz} = \frac{1}{2}\left(\frac{\partial u}{\partial z} + \frac{\partial w}{\partial x}\right), \quad \epsilon_{kk} = \epsilon_{xx} + \epsilon_{zz}. \tag{28}$$

Solving the four coupled governing equations [Eqns.(18), (19), (20), (21)], we obtain the spatiotemporal evolution of the saturation, displacements and pressure field. To quantify the vulnerability of firn to hydrofractures based on Eqn. (7), the model outputs the infiltration-induced change of horizontal effective stress as follows:

$$\delta\sigma'_{xx} = \delta\sigma_{xx} + b\delta p = \frac{3K\nu}{1+\nu}\epsilon_{kk} + \frac{3K(1-2\nu)}{1+\nu}\epsilon_{xx}. \qquad (29)$$

2.2.4 Initial and Boundary Conditions

The model solves the infiltration-induced pressure and stress changes in the porous firn layer, where $0 \leq x \leq L$, and $0 \leq z \leq H$ (Figure 2). Water flows into the crevasse, the tip of which has an opening L_{crev}. Water infiltrates into the porous firn layer via the crevasse tip at either a constant height, H_w, or a constant velocity, V_{inj}. We initialize the model by specifying $u(x,z,0) = w(x,z,0) = p(x,z,0) = 0$. The water saturation is zero everywhere except at the crevasse tip, where it is kept at $S_w = 1$ as follows:

$$S_w(x \leq L_{\mathrm{crev}}, 0, t) = 1, S_w(x > L_{\mathrm{crev}}, 0, t) = S_w(x, z > 0, 0) = 0. \qquad (30)$$

We consider the stress (or displacement) and pressure (or flow rate) boundary conditions on the domain area. On the left boundary ($x = 0$), axis of symmetry requires that $\frac{\partial}{\partial x} = 0$, and horizontal displacement equals zero. On the right boundary, we assume it is far from the crevasse tip and unaffected by the infiltration. On the bottom boundary where the firn layer touches the impermeable, rigid ice column, the displacements and vertical water flow rate are zero. On the top boundary, when the water surface height exceeds the ice slab height (e.g. when a lake overlies the ice slab), the lake depth adds to the lithostatic stresses. Otherwise the overlying ice slab provides constant lithostatic stresses. The vertical water flowrate is zero everywhere except at the crevasses, where either $p = \rho_w g H_w$ or $q_{w,z} = V_{\mathrm{inj}}$. The boundary conditions are summarized as follows:

$$\begin{aligned}
&u|_{x=0} = \frac{\partial w}{\partial x}|_{x=0} = \frac{\partial p}{\partial x}|_{x=0} = \frac{\partial S_w}{\partial x}|_{x=0} = 0,\\
&u|_{x=L} = w|_{x=L} = p|_{x=L} = 0,\\
&u|_{z=H} = w|_{z=H} = q_{w,z}|_{z=H} = 0,\\
&\delta\sigma'_{xx}|_{z=0} = \delta\sigma'_{zz}|_{z=0} = 0,\\
&q_{w,z}|_{z=0}(x > L_{\mathrm{crev}}) = 0,\\
&p|_{z=0}(x \leq L_{\mathrm{crev}}) = \rho_w g H_w \quad \text{or} \quad q_{w,z}|_{z=0}(x \leq L_{\mathrm{crev}}) = V_{\mathrm{inj}}.
\end{aligned} \qquad (31)$$

2.2.5 Model Parameters

The four poroelastic constants in the model are the drained bulk modulus K, the drained Poisson ratio ν, the Biot coefficient b, and the Biot modulus M of the firn layer. We calculate the Biot coefficient from the relationship $b = 1 - \frac{K}{K_s}$ (Coussy, 2004), where K_s is the bulk modulus of the ice grain. The Biot modulus of the porous firn, M, is related to fluid and firn properties as $\frac{1}{M} = \phi S_w c_w + \phi(1-S_w)c_a + (b-\phi)c_s$ (Coussy, 2004), which is a spatiotemporal variable as water penetrates into the firn layer. A summary of the modeling parameters is given in Table 1.

Table 1. Modeling parameters for the 2D, two-phase poroelastic continuum model

Symbol	Value	Unit	Variable
L	30	m	Length of the firn layer
H	30	m	Height of the firn layer
L_{crev}	2	m	Half of the opening of the crevasse
H_w	10	m	Water height above the firn layer
z_0	1	m	Depth of the injection port
V_{inj}	0.05	m/s	Water infiltration rate
c_w	5×10^{-10}	Pa^{-1}	Water compressibility
c_a	7×10^{-6}	Pa^{-1}	Air compressibility
K	4	GPa	Bulk modulus of the firn layer
K_s	8	MPa	Bulk modulus of the ice grain
ν	0.3		Poisson ratio of the firn layer
b	0.5		Biot coefficient of the firn layer
η_w	0.001	Pa·s	Injecting water viscosity
η_a	1.8×10^{-5}	Pa·s	Air viscosity
ϕ	0.2		Porosity of the firn layer
k_0	10^{-9}	m^2	Intrinsic permeability of the firn layer
ρ_s	917	kg/m^3	Density of the ice grain
ρ_w	997	kg/m^3	Density of water
ρ_a	1.23	kg/m^3	Density of air

2.2.6 Numerical Implementation

We use a finite volume numerical scheme to solve the four coupled governing equations [Eqns. (18), (19), (20),(21)]. We partition the coupled problem and solve two sub-problems sequentially: the coupled flow and mechanics, and the transport of water saturation. We first fix the water saturation, and solve the coupled flow and mechanics equations [Eqns. (18), (20), (21)] simultaneously using implicit time discretization. Then we solve the water transport equation [Eqn. (19)] with prescribed pressure and displacement fields. The convergence and mesh independence analysis is included in the Appendix [Figure 12]. The modeling results reach convergence with the mesh size dx=dz=0.5 m, which is adopted for all the simulation presented here.

3. Results

3.1 Spatiotemporal evolution of pressures and stresses

We compare modeling results for water infiltration with two different boundary conditions at the crevasse tip: constant pressure (H_w = 10 m), and constant flow rate (V_{inj} = 0.05 m/s) [Figure 3&4]. In both cases, water infiltrates into the porous firn layer due to the pressure gradient and gravity, resulting in a quarter-elliptical shape for the water saturation profile [Figure 3(a)]. The temporal evolution of the pore pressure field indicates that pressure diffuses within the water phase, as the air

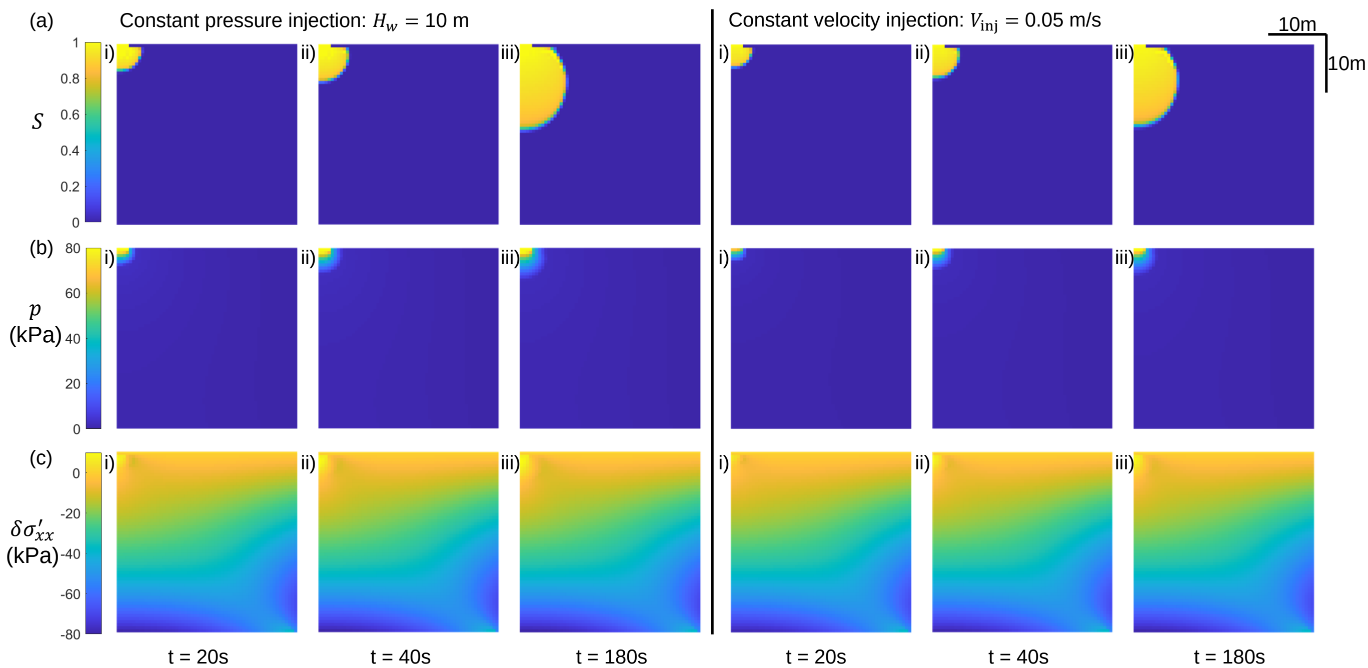

Fig. 3. Modeling results for the water infiltration with H_w = 10 m (left panel), V_{inj} = 0.05 m/s (right panel) in the domain $0 < x < L, 0 < z < H$. A sequence of snapshots shows the spatiotemporal evolution of (a) water saturation field, $S_w(x, z, t)$, (b) pore pressure field, $p(x, z, t)$, and (c) infiltration-induced horizontal effective stress change, $\delta\sigma'_{xx}(x, z, t)$. Infiltration time t=20s, 40s, 180s from snapshot i), ii) to iii).

viscosity is negligible compared with water [Figure 3(b)]. The viscous dissipation is constrained within a certain depth, below which the water flow becomes purely gravity-driven. Figure 3(c) shows the spatiotemporal evolution of the infiltration-induced horizontal effective stress change ($\delta\sigma'_{xx}(x, z, t)$). At the crevasse tip, the firn is under the maximum tensile effective stress, which makes it the most vulnerable place for hydrofracturing (see the fracture criterion in Eqn. (7)).

We also present the temporal evolution of the infiltration-induced pore pressure ($P_{\text{inj}}(t)$) and the effective stress ($\delta\sigma'_{xx}(t)$) at the crevasse tip [Figure 4]. For the constant velocity injection condition, it takes some time for the injection pressure to build up [Figure 4(a)], and thus the water invading front is slightly delayed compared with the constant pressure condition [Figure 3]. With either constant pressure or constant flow rate as the boundary condition, the tensile effective stress at the crevasse tip experiences a logarithmic growth in time with a fast increase in the first 30 seconds [Figure 4(b)]. To avoid boundary effects, we terminate the simulation when water infiltrates into half of the domain depth, and take the corresponding pressure (δp) and tensile effective stress at the crevasse tip ($\delta\sigma'_{xx,\max}$) for the following scaling analysis.

3.2 Analytical model

3.2.1 Scaling between $\delta\sigma'_{xx,max}$ and δp

To check whether fracture initiates in the porous firn layer during meltwater infiltration, we focus on the stress and pressure changes at the crevasse tip, where has been shown to be the most vulnerable place. To implement the fracture criterion in Eqn. (7) more efficiently, we develop a scaling relationship

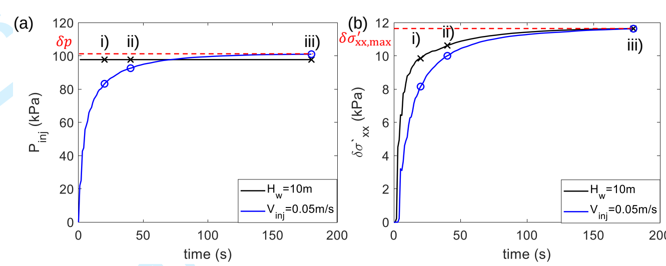

Fig. 4. Modeling results for the water infiltration with H_w = 10 m (black line) and V_{inj} = 0.05 m/s (blue line). Time evolution of (a) injection pressure $P_{\text{inj}}(t)$ at the crevasse tip, and (b) infiltration-induced horizontal effective stress change at the crevasse tip $\delta\sigma'_{xx}(t)$. We use their maximum values (δp, $\delta\sigma'_{xx,\max}$) to evaluate the vulnerability of the porous firn layer to hydrofracturing. The markers indicate times for the snapshots shown in Figure 3: t=20s, 40s, 180s in sequence.

between $\delta\sigma'_{xx,max}$ and δp, which dictates how much of the infiltration-induced pore pressure change is transmitted to the solid skeleton. We recall the poroelasticity equation on the effective stress [Eqn. (1)], and propose a scaling law for the infiltration-induced horizontal effective stress change at the crevasse tip as follows:

$$\delta\sigma'_{xx,max} = \delta\sigma_{xx,max} + b\delta p = -\gamma(b\delta p) + (b\delta p) = \beta(b\delta p). \quad (32)$$

where we assume the horizontal total stress change is linearly proportional to the pore pressure change with a numerical pre-factor $0 < \gamma < 1$, and is negative as it is compressive. We then conduct a series of simulations to determine the numerical pre-factor $0 < \beta < 1$.

3.2.2 Analytical expressions of $\delta\sigma'_{xx,max}$ and δp

To find the modeling parameters that impact the stresses, we develop analytical predictions on δp under the two boundary conditions. For the constant pressure injection at the crevasse tip, the pressure change is equal to the hydrostatic water pressure, $\delta p = \rho_w g H_w$. For the constant velocity injection at the crevasse tip, we derive δp from fluid continuity and Darcy's law. We assume that above a certain water infiltration depth H_0, whose expression is derived later, water infiltrates much faster than the hydraulic conductivity of the firn. Therefore gravity is negligible and water invades in an approximately radially symmetric manner [Figure 3(i)(ii)]. From the fluid continuity, we obtain:

$$V_{\text{inj}} L_{\text{crev}} = V(z)\frac{\pi z}{2} \rightarrow V(z) = \frac{2V_{\text{inj}}L_{\text{crev}}}{\pi}\frac{1}{z}. \quad (33)$$

where $V(z)$ is the Darcy velocity for water at depth z. At $z = H_0$, the water velocity decays to the gravity-driven flow rate, which is also the hydraulic conductivity of water flow in porous firn. We derive the expression for H_0 as follows:

$$V(H_0) = V_{\text{grav}} = \frac{\rho_w g k_0}{\mu_w} \rightarrow H_0 = \frac{2V_{\text{inj}}L_{\text{crev}}\eta_w}{\pi\rho_w g k_0}. \quad (34)$$

Pore pressure diffuses from the crevasse tip (z_0) to H_0, below which the flow becomes gravity-driven, resulting in the observed quarter-elliptical shape of the water invading front. We calculate the pressure diffusion from z_0 to H_0 by Darcy's law:

$$V(z) = -\frac{k_0}{\eta_w}\frac{\partial p}{\partial z} \rightarrow \int_{z_0}^{H_0} -\frac{\eta_w}{k_0}V(z)\partial z = \int_{\delta p}^{0}\partial p,$$
$$\rightarrow \delta p = \frac{2}{\pi}\frac{\eta_w V_{\text{inj}}L_{\text{crev}}}{k_0} ln(\frac{H_0}{z_0}). \quad (35)$$

Note that Eqn. (35) applies to the condition when the water velocity decays to the gravity-driven flow rate before the invading front reaches approximately half of the domain depth. For an unrealistically large crevasse opening or water injection velocity at the crevasse tip, the invading front keeps expanding in a quarter-circular shape, and H_0 in Eqn. (35) is replaced by the depth when we terminate the simulation ($\frac{H}{2}$ in this case). We include the analysis of large injection velocity or crevasse opening in the Appendix [Figure 13]. However, the large water pressure induced there (in the range of MPa) is not physical as it should have been capped by hydrostatic water pressure, $\rho_w g H_w$. Combining equations (32),(34),and (35), we obtain the theoretical prediction of $\delta\sigma'_{xx,\max}$ at the crevasse tip for the two boundary conditions:

$$\delta\sigma'_{xx,max} = \beta(b\delta p) - \frac{\nu}{1-\nu}\rho_w g\langle H_w - H_i\rangle,$$
$$\delta p = \begin{cases} \rho_w g H_w, \text{ with a constant } H_w, \\ \frac{2}{\pi}\frac{\eta_w V_{\text{inj}}L_{\text{crev}}}{k_0} ln(\frac{2}{\pi\rho_w g z_0}\frac{\eta_w V_{\text{inj}}L_{\text{crev}}}{k_0}), \text{ with a constant } V_{\text{inj}}. \end{cases} \quad (36)$$

where $\langle x\rangle = \max(x, 0)$ follows the rule of Macaulay bracket. To validate Eqn. (36), we conduct a serious of simulation under both boundary conditions by varying the modeling parameters, including $b, H_w, V_{\text{inj}}, L_{\text{crev}}$ and k_0. We set $H_w < H_i$ in all simulations with a constant pressure boundary condition. Figure 5 presents the dependence of $\delta\sigma'_{xx,\max}$ on the modeling parameters, where the red dashed line represents the analytical prediction from Eqn. (36) with the numerical pre-factor β fitted to be 0.22. For all constant injection velocity simulations, the simulated δp as a function of $\frac{\eta_w V_{\text{inj}}L_{\text{crev}}}{k_0}$ agrees with the theory [Eqn. (35); red dashed line in Figure 6(a)] without fitted parameters.

Finally, we combine all the simulation data onto a single plot to show the robustness of the proposed scaling, which is universal across a range of parameters and both boundary conditions: $\delta\sigma'_{xx,\max} = \beta(b\delta p)$, where $\beta = 0.22$ [Figure 6(b)]. Note that to cause fracture we need the maximum effective stress $\sigma'_{xx,max} \equiv \sigma'_{xx,0} + \delta\sigma'_{xx,max}$ to exceed the tensile strength σ'_t, where $\sigma'_{xx,0} = -\frac{\nu}{1-\nu}\rho_i g H_i$ is the initial compressive effective stress and $\delta\sigma'_{xx,\max} = \beta(b\delta p)$ is the maximum changes of effective stress due to water injection. The analytical prediction of the final forms of the effective stress for the constant pressure cases are summarized in Figure 7, which are used for the following Greenland firn stability analysis.

3.3 Physical Limits

Eqn. (36) provides different forms for the maximum effective stress in the firn depending on whether a constant pressure or constant injection velocity is assumed. Before applying this model to study the vulnerability of ice slab regions to hydrofracture, it is important to consider which boundary condition is most consistent with physical conditions on the ice sheet.

The constant pressure boundary condition straightforwardly represents a static water load in a partially or fully water-filled crevasse. It does not directly account for transient processes, such as water level fluctuations within a crevasses as water flows in from surface runoff or out through the permeable firn. However, by exploring the induced stresses for a range of water levels, we can constrain the plausible range of the maximum effective stress in the firn layer.

It is tempting to think of the constant injection velocity boundary condition as representing the transient case where water is flowing into the crevasse at a constant rate. However, this is not a good analogy. As Figure 4 shows, a constant injection rate leads to roughly logarithmic increase in pressure with time, as more water is forced into the firn per time step than can be evacuated from the injection point due to the relatively low intrinsic permeability of the firn. However, a crevasse is not a closed system and the top remains open to the atmosphere. Therefore, when the rate of water injection into the crevasse exceeds the rate at which water can flow out through the firn, continuity of mass and pressure require that the water will start to fill the crevasse, rather than increase pressure in the firn layer. As a result, this boundary conditions leads to artificially high estimates of firn pore pressure and, by extension, maximum effective stress, because our simulations assume a closed system and do not allow for backflow into the

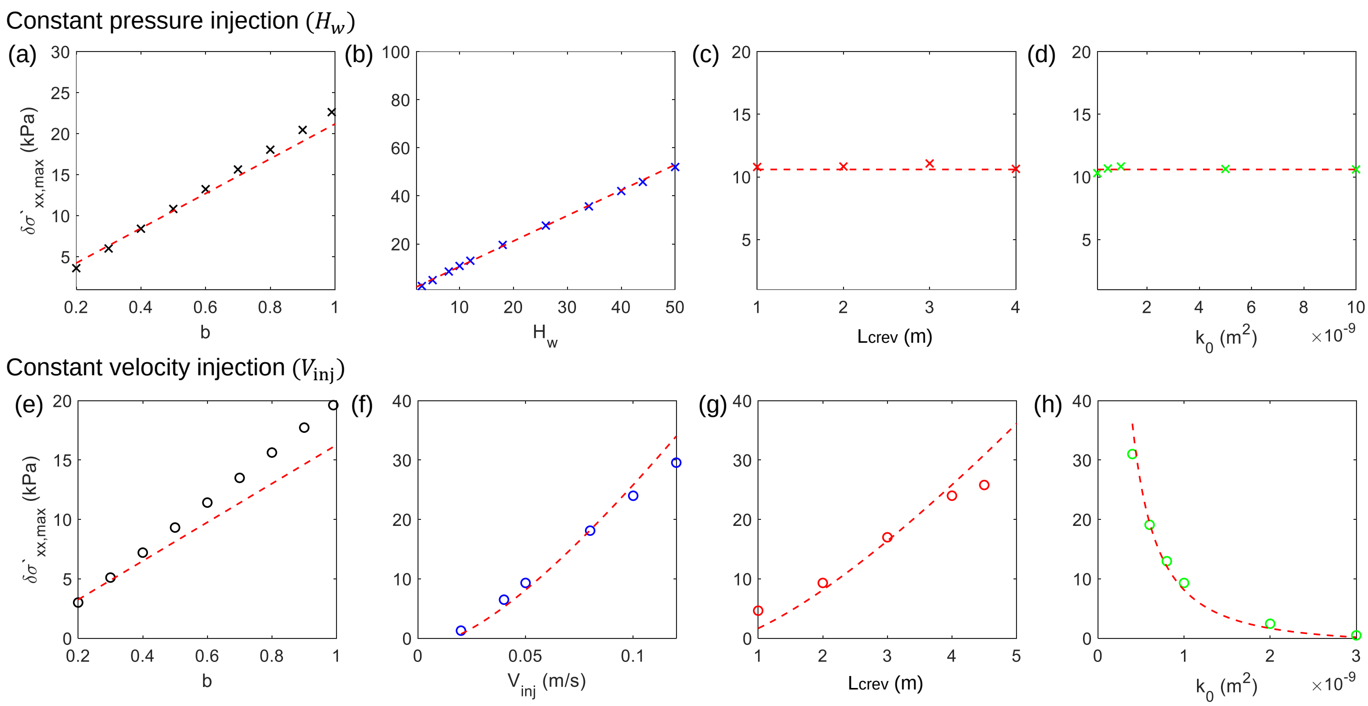

Fig. 5. The dependance of $\delta\sigma'_{xx,max}$ on modeling parameters (b, H_w, V_{inj}, L_{crev}, k_0) for the water infiltration with a constant injection pressure (top panel, (a)∼(d)) and a constant injection velocity (bottom panel, (e)∼(h)). On the top panel, H_w = 10 m except in (b), and on the bottom panel, V_{inj} = 0.05 m/s except in (f). The markers represent simulation results, and the dashed red line represents analytical prediction from Eqn. (36) with β = 0.22.

open crevasse. Therefore, we caution that the constant injection rate equations should not be used to calculate firn stresses. However, the constant injection rate model does provide an important relationship between pressure and injection velocity that we will later exploit to qualitatively estimate whether crevasses may fill with water, given typical stream flow rates into fractures. Figure 7 summarizes the final constant pressure scenarios that we use to calculate the maximum effective stress in the firn.

4. Applications to the Greenland Ice Sheet

We now apply the analytical model developed in Section 3 to assess the vulnerability of Greenland's ice slab regions to hydrofracture. To do this, we seek answer the following questions:

1. Given typical firn conditions in Greenland, will fractures in ice slabs fill with water?
2. If so, is the stress induced by water loading increased or decreased by the presence of a porous firn layer?

The first question is important because, as water flows into the top of an ice slab crevasse, either from distributed hillslope flow or where a stream intersects the fracture, it will also flow out of the fracture tip into the permeable firn. If water can be evacuated into the firn at a similar rate as the rate at which it enters the crevasse, the crevasse will not fill with water and there will be no additional hydrostatic stress that might drive hydrofracture. However, if the rate of infiltration into the firn is smaller than the rate of injection into the crevasse, the water level will rise within the crevasse. In this scenario, the second question becomes relevant, and we can apply Equation 36 to determine whether, or under what conditions, the maximum effective stress induced in the firn layer would be sufficient to initiate fracture.

4.1 Mechanical and Hydraulic Parameters

To calculate maximum effective stress from the equations detailed in Figure 7, we must first define reasonable values for the physical, mechanical, and hydraulic parameters of the ice slab-firn system in our area of interest. Unfortunately, given the large spatial extent of ice slab regions, the sparsity of subsurface observations within them, and the uncertainty in the few available measurements, it is difficult to choose a single representative value for any of these parameters. Therefore, we take a Monte Carlo simulation approach to this problem. For each variable, we define an empirical distribution of reasonable values using a compilation of in situ, laboratory, and remote sensing measurements reported in the literature. For the hydraulic and mechanical properties, which have never been measured directly in these regions, we use various empirical relations to define these properties as a function of firn density. Table 2 lists these unknown variables, the distributions we assign to them or the relation from which we calculate them, and the sources on which we base these distributions or relations.

The relation between open porosity and firn permeability is taken from Adolph and Albert (2014), which defined a power law relation between firn density and air permeability based

Table 2. Monte Carlo Simulation Parameters

Variable	Distribution/Relation	Unit	Sources
ρ_i	$\mathcal{N}(873, 25)$	kgm^{-3}	Machguth and others (2016)
ρ_f	$\mathcal{U}[550, 800]$	kgm^{-3}	Machguth and others (2016); Macferrin and others (2022)
H_i	Empirical distribution of all radar-observed ice slab thickness in Greenland	m	MacFerrin and others (2019)
H_w	$\mathcal{U}[0, H_i], (H_w \leq H_i)$ OR $\mathcal{U}[H_i + 0.1, H_i + 40], (H_w > H_i)$	m	Culberg and others (2022)
K	$K_\mu = (1.844 \times 10^{-5})\rho_f^2 - 0.006956\rho_f - 0.0606$; $\sigma_K = 0.436$	GPa	Schlegel and others (2019); King and Jarvis (2007); Smith (1965)
K_s	$\mathcal{N}(8.5, 0.28)$	GPa	Sayers (2021)
b	$b = 1 - \frac{K}{K_s}$	dimensionless	Biot (1941)
ν	$\nu_\mu = 0.0002888\rho_f + 0.1005$; $\sigma_\nu = 0.0376$	GPa	Schlegel and others (2019); King and Jarvis (2007); Smith (1965)
k_0	$k_0 = 10^{-7.29}\phi_0^{3.71}$	m^2	Adolph and Albert (2014)

*Note that $\mathcal{N}(\mu, \sigma)$ denotes a normal distribution with mean μ and standard deviation σ and $\mathcal{U}[a, b]$ denotes a uniform distribution over the values from a to b (inclusive).

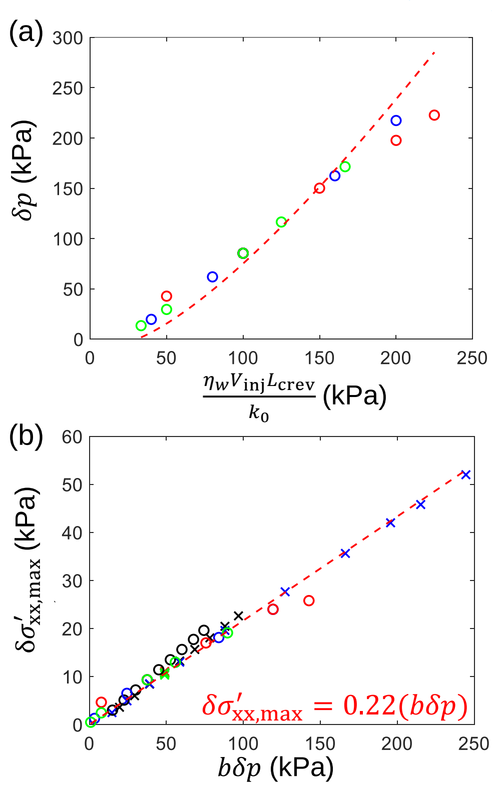

Fig. 6. (a) The scaling between the infiltration-induced pore pressure change at the crevasse tip (δp) and viscous pressure ($\frac{\eta_w V_{\mathrm{inj}} L_{\mathrm{crev}}}{k_0}$) from the water infiltration with a constant injection velocity. The markers represent simulation results, and the dashed red line represents analytical prediction from Eqn. (36). (b) The scaling between $\delta\sigma'_{\mathrm{xx,max}}$ and $b\delta p$. Markers represent all simulation data in Figure 5 from water infiltration with a constant injection pressure or constant injection velocity. The dashed red line represents the analytical prediction: $\delta\sigma'_{\mathrm{xx,max}} = \beta\delta p$ (Eqn. (36)), with the prefactor β fitted to be 0.22.

on measurements from firn core samples collected at North GRIP ice core drill site. We define our own relations between firn density and the mechanical parameters – Poisson's Ratio (ν) and Biot coefficient (b) – due to the lack of reports in the literature. The Poisson's Ratio has been measured with ultrasonic wave velocities at the laboratory scale and active seismic investigations at the field scale. We collate data sets from Schlegel and others (2019), King and Jarvis (2007), and Smith (1965) and use Monte Carlo simulation to build an expanded set of data points that cover the reported uncertainty for each measured data point. We then calculate the best linear fit between firn density (ρ_f) and ν using this expanded data set (Supp. Fig. 2) and define the uncertainty to be the one half of the 68% prediction interval on the measurements (reported as σ_ν in Table 2). The Biot coefficient is defined as a function of the ratio between the bulk modulus of the firn (K) and single grain elastic stiffness of ice (K_s). We define a relation between ρ_f and K in the same way as we did for ν, but this time using a quadratic fit to bulk modulus data compiled from the same sources (Supp. Fig. 1).

For each Monte Carlo simulation, we first draw ρ_i, ρ_f, L_{crev}, K_s, and H_i from the distributions defined in Table 2. If $H_w \leq H_i$ in our simulation scenario, we then draw H_w from the distribution $\mathcal{U}[0, H_i]$. If $H_w > H_i$, we draw H_w from the distribution $\mathcal{U}[H_i+0.1, H_i+40]$. We use the randomly selected value of ρ_f to calculate K, ν, or k_0 as appropriate. For example, K is drawn from a distribution defined as $\mathcal{N}(K_\mu(\rho_f), \sigma_K)$ and then used to calculate b directly. For all the analyses that follow, we run 1,000,000 iterations of the Monte Carlo simulation, equivalent to solving the equations in Figure 7 for a million different plausible configurations of an ice slab–firn system. The output of this simulation process is a distribution of the physically plausible range of maximum effective stress in the firn layer (or whatever variable we are solving for), given what we know about conditions in Greenland's ice slab regions.

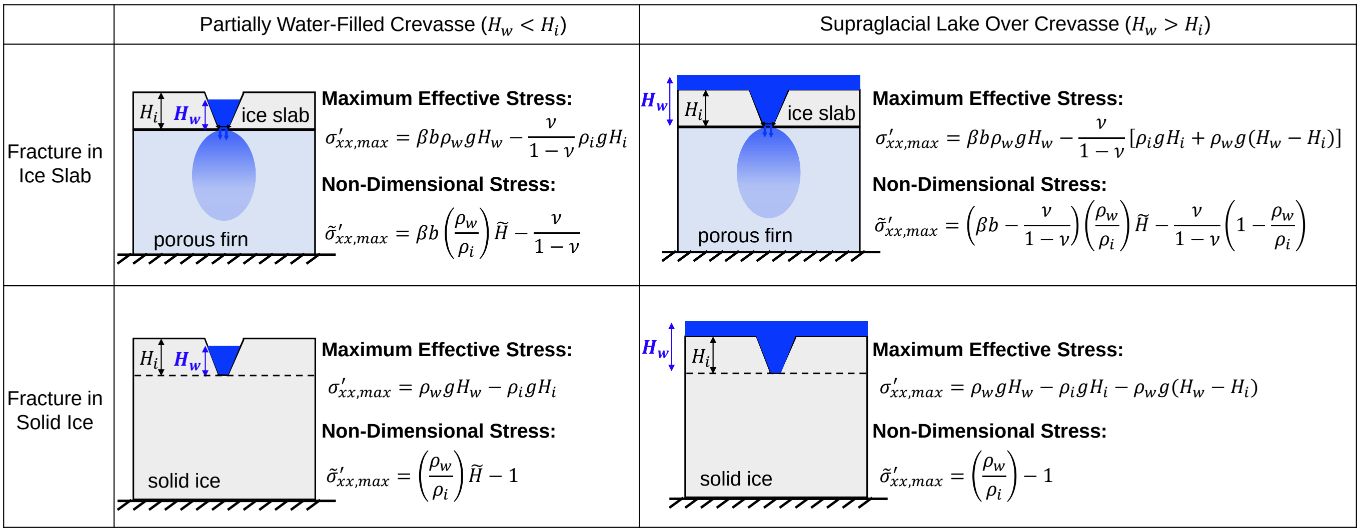

Fig. 7. The theoretical prediction of the maximum effective stress at the crevasse tip $\sigma'_{xx,\max}$. We present $\sigma'_{xx,\max}$ in both dimensional and dimensionless forms.

4.2 *Rate of Crevasse Filling*

To determine whether fractures in ice slabs can fill with water, we start with the constant injection velocity solution in Equation 36 which provides a relationship between pressure and firn infiltration velocity. This equation shows that the change in pore pressure is related to the injection velocity, crevasse opening width, and firn permeability. Since the crevasse is open to the atmosphere at its top, we know that the maximum possible pressure change in the firn would be the hydrostatic pressure induced by a water-filled crevasse. Therefore, we set Eqn. 36 equal to this hydrostatic pressure to estimate the maximum rate at which water can infiltrate into the firn.

$$\rho_w g H_w = \left(\frac{2\eta_w L_{crev}}{\pi k_0}\right) V_{inj} \ln\left[\left(\frac{2\eta_w L_{crev}}{\pi \rho_w g z_0 k_0}\right) V_{inj}\right] \quad (37)$$

Using the Monte Carlo approach described in Section 4.1, we numerically solve Eqn. 37 to compute a distribution of plausible infiltration rates (V_{inj}) into the firn beneath ice slabs.

We compare this distribution of infiltration rates to field measurements of supraglacial river and stream discharge to assess the balance between water flowing into and out of crevasse. For this purpose, we reduce the system to two-dimensions and calculate discharge into the firn as follows:

$$Q_{firn} = V_{inj} L_{crev} \quad (38)$$

We compare Q_{firn} ($m^2 s^{-1}$) to field observations of supraglacial stream and river discharge collected in the ablation zone of Southwest Greenland. Gleason and others (2016) measured width, depth, and discharge at 38 locations on a series of small streams – generally, less than 3m wide and 0.3 m deep. We calculate an equivalent 2D discharge by dividing the measured discharge by the stream width. Smith and others (2015) developed the power law relation between stream width (w) and discharge (Q) shown in Eqn. 39 based on field measurements in Southwest Greenland. They applied this relationship to estimate stream discharge from WorldView 1-3 imagery of the same area, thus calculating discharge volumes for 532 streams where they terminated into moulins.

$$w = 3.48Q^{0.54} \quad (39)$$

To rescale their discharge estimates ($m^3 s^{-1}$) to an equivalent two-dimensional discharge ($m^2 s^{-1}$) that can be compared directly to Q_{firn}, we divide the stream discharge volumes reported in Smith and others (2015) by the stream width calculated from Eqn. 39. The rescaling relation is given below in Eqn. 40.

$$Q_{surf} \approx Q/w = 0.287Q^{0.46} \quad (40)$$

Figure 8 shows the results of this analysis. The blue histogram shows the rate at which water would drain out of a crevasse in an ice slab into the underlying firn, and the yellow and red histograms show that rate at which water can drain into the crevasse from the surface. We see two distinct regimes. Q_{surf} and Q_{firn} are similar for the streams with the lowest discharge rates and crevasses with the largest openings, highest pressures, and most permeable underlying firn. This suggests that where crevasses are fed by small streams or hillslope flow, no hydrofracture will occur because water drains into the firn as quickly as it enters the crevasse, and therefore no hydrostatic stress is induced by water within the crevasse itself. However, we also see a wide range of stream and river discharge rates that are significantly greater than the rate at which water can drain out of a crevasse into the firn. In this second regime, the crevasse will fill with water, leading to an additional hydrostatic load that might be sufficient to vertically propagate the crevasse into the firn layer. Therefore, we address the second question – does hydrostatic loading of an ice slab crevasse induce sufficient stress in the firn layer to initiate fracture?

4.3 *Maximum Effective Stress in the Firn Layer*

4.3.1 *Effects of Water Depth*

We use the same Monte Carlo simulation approach to estimate the physically plausible distribution of maximum effective stress

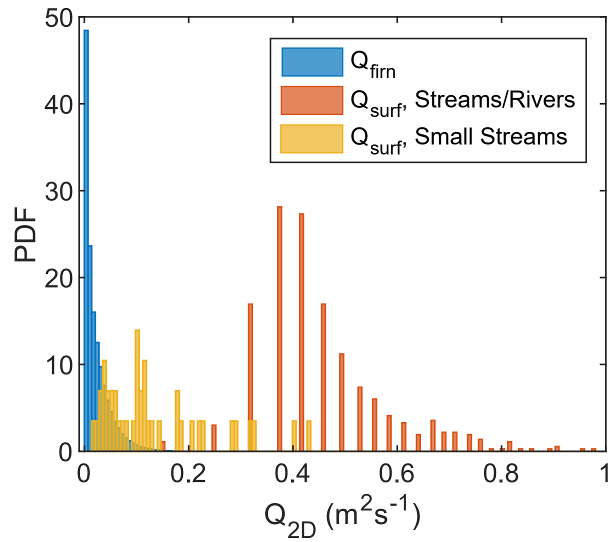

Fig. 8. Comparison of the rate of water infiltration into the firn from a crevasse tip versus the rate at which surface streams may feed water into a crevasse. Blue bars show the distribution of firn water infiltration rates in response to a range of pressures equivalent to that induced by a partially water-filled crevasse. Yellow bars show small stream discharge values measured in the ablation zone of Southwest Greenland. Red bars show large stream and small river discharge values measured in the same region. In most cases, water infiltrates out of the crevasse tip more slowly than water enters the crevasse opening by stream flow, suggesting that many crevasses will partially fill with water.

that might be induced in the firn by a water-filled crevasse in an ice slab. We compare these distributions to the distribution of effective stress (equal to total stress) at the fracture tip of an equivalent system in a solid ice column. We consider two scenarios: a partially water-filled crevasse ($0 \leq H_\mathrm{w} \leq H_\mathrm{i}$) and a supraglacial lake overtop a crevasse ($H_\mathrm{w} > H_\mathrm{i}$), where the surface area of the fracture is assumed to be negligible when compared to the total extent of the lake. By comparing the maximum effective tensile stress in the firn layer to the total stress at the crevasse tip in solid ice, we can evaluate whether the presence of the firn layer beneath ice slabs leads to lower or higher stress than solid ice hydrofracture case. Figure 7 summarizes the scenarios and equations we use for this analysis.

Figure 9 shows the result of this analysis, highlighting three regimes with distinct behaviors. When the water level in the crevasse is less than $\left(\frac{\rho_i}{\rho_w}\right) H_i$, the maximum effective stress is quite similar, regardless of whether there is an underlying firn layer or not. In fact, in some cases, the maximum effective stress is greater when a firn layer is present, although both the effective stress is net compressive in all cases. However, once $H_w > \left(\frac{\rho_i}{\rho_w}\right) H_i$, there is a distinct shift in behavior. The effective stress in the solid ice system is always tensile, but the effective stress in the ice slab-firn system remains compressive and takes on a similar range of values as in the first regime. In the case of a supraglacial lake overtop a crevasse ($H_w > H_i$), the effective stress in the solid ice system is always tensile as well. However, for the ice slab-firn system, the range of maximum effective stresses becomes significantly more compressive than in the case of a water-filled crevasse alone.

We now define a non-dimensional maximum effective stress and non-dimensional water height as follows and rescale the equations in Figure 7.

$$\tilde{\sigma}'_{xx,max} = \frac{\sigma'_{xx,max}}{\rho_i g H_i} \tag{41}$$

$$\tilde{H} = \frac{H_w}{H_i} \tag{42}$$

Figure 7 give the non-dimensional and simplified forms of the equations and Figure 10 shows the results of plotting these equations as function of $\tilde{H}$.

In the non-dimensional form of the equations, we can think of the first term – some constant multiplied by $\tilde{H}$ – as the hydrostatic term that describes how the maximum effective stress changes as the water pressure in the crevasse changes. The second term is a lithostatic term that describes the background state of stress in the system. Before water is added to the crevasse, the maximum effective stress in the firn is lower than in solid ice, because the firn's lower Poisson's Ratio means that less of the overburden-induced vertical stress is transmitted horizontally. However, as water begins to fill the fracture, the maximum effective stress increases more slowly in the ice slab-firn system compared to the solid ice system, because only a portion of the hydrostatic stress is transferred to the solid skeleton, with the remainder being accommodated by an increase in pore pressure. As a result, once the water level in the crevasse exceeds roughly $H_w > 0.6H_i$, the effective stress at the fracture tip in solid ice exceeds the maximum effective stress experienced by the firn. The exact point of this crossover can be calculated as a function of ν and b as shown in Eqn. 43.

$$\tilde{H} = \left(\frac{1-2\nu}{1-\nu}\right)\left(\frac{1}{1-\beta b}\right)\left(\frac{\rho_i}{\rho_w}\right) \approx 0.6 \tag{43}$$

Once $\tilde{H} \geq \frac{\rho_i}{\rho_w}$, the effective stress in the solid ice system will always be tensile. This is the critical conclusion of classical hydrofracture analyses in glaciology – that, due to the density difference between water and ice, a water-filled crevasse will always be in net tension and can propagate unstably (van der Veen, 2007; Lai and others, 2020). However, in the presence of an underlying firn layer, this transition is never reached and the maximum effective stress always remains compressive, due to the mitigating effect of pore pressure.

In the case of a supraglacial lake, where $H_w > H_i$, the classical solution for solid ice hydrofracture is identical to the solution for a completely water-filled crevasse and is independent of the depth of the lake. This is the case because the additional overburden from the lake contributes equally to the lithostatic and hydrostatic terms, so that the effective stress simply remains a function of the density difference between the water and ice in the crevasse. However, in the presence of an underlying firn layer, the maximum effective stress is significantly reduced by the presence of an overlying supraglacial lake and in fact decreases linearly as lake depth increases. The

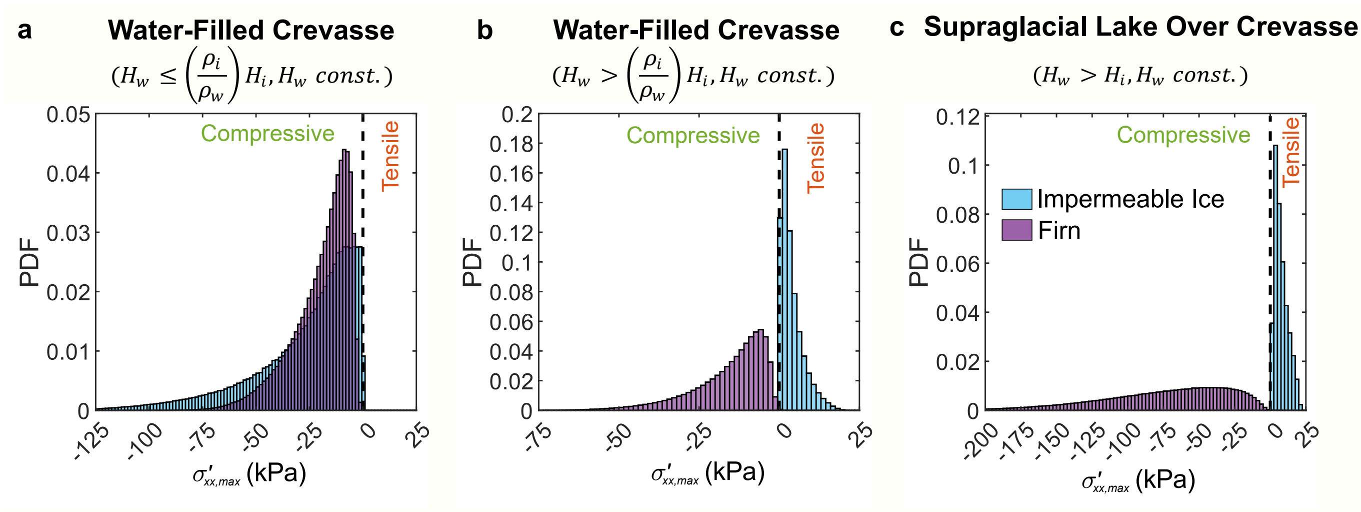

Fig. 9. Physical plausible distributions of maximum effective stress in the firn layer, following Eqn. 36 (purple bars). We use a range of values for b and ν based on field and laboratory observations in Greenland. Blue bars show the maximum effective stress at the crack tip in an equivalent solid ice column. a) Effective stress in a partially water-filled crevasse. The ice slab-firn and solid ice systems have a similar range of effective stresses, as reduced overburden in the ice slab-firn scenario balances the complete transmission of hydrostatic stress in the solid ice system. b) Effective stress is an almost fully water-filled crevasse. Effective stress in the solid ice system is tensile, as hydrostatic stress exceeds lithostatic stress. Effective stress in the ice slab-firn system remains compressive, as pore pressure accommodates much of the hydrostatic stress. c) Effective stress for a supraglacial lake overtop a crevasse. In a solid ice system, there is no change in the effective stress distribution from a fully water-filled crevasse. In the ice slab-firn system, the effective stress becomes more compressive, due to the additional lithostatic stress imposed by the water load in the lake around the fracture.

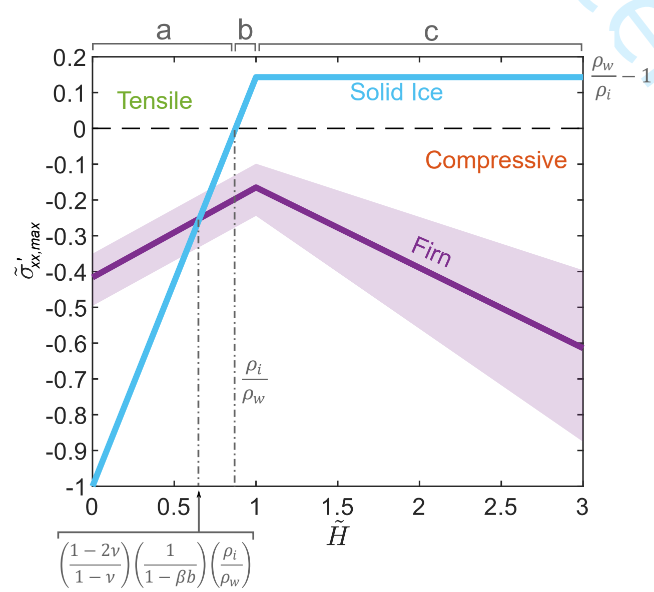

Fig. 10. Non-dimensional analysis of maximum effective stress ($\tilde{\sigma}'_{xx,max}$) as a function of water height within the crevasse ($\tilde{H}$). For the ice slab-firn system, shaded areas show the range of possible values given plausible firn densities, with the solid line showing an "average" behavior for the Greenland Ice Sheet. Labels a-c along the top axis show correspond to the regimes shown separately in panels a-c of Figure 9.

system behaves in this way because the overlying lake water contributes more to increasing the lithostatic stress acting to close the fracture than it does to increasing the hydrostatic stress, due to the competing influence of the Poisson's Ratio and Biot coefficient on the transfer of stress to the firn skeleton.

4.3.2 *Effects of Firn Porosity*

Since ν and b are both a function of firn porosity, we also explore the change in non-dimensional maximum effective stress as a function of firn porosity and non-dimensional water height. We plot the same data points shown in Figure 9 in firn porosity vs $\tilde{H}$ space, taking the median simulation values in each 2D bin (Figure 11). For a partially or fully water-filled crevasse, the effective stress increases as the water height increases, due to the greater hydrostatic pressure. Effective stress also increases a firn porosity increases. Softer, more porous firn has a higher Biot coefficient and therefore a stronger fluid-solid coupling, so more of the hydrostatic stress is felt by the solid skeleton. More porous firn is also more compressible and has a lower Poisson's Ratio, so less of the lithostatic stress is transmitted horizontally and can act to close the crevasse. Instead, the firn compacts vertically under the overburden. In the case of a supraglacial lake over a crevasse, we instead find that an increase in lake depth reduces the effective stress due to the increasing influence of the lithostatic stress component. As expected, effective stress still increases as firn porosity increases, but this influence is more significant at greater lake depths, since it reflects how the coupling between hydrostatic stress and maximum effective stress is modulated by the Biot coefficient. Overall, we find that a low porosity, stiff firn matrix will be the most stable.

5. Discussion

Our results demonstrate that the presence of a porous firn layer underneath Greenland's ice slabs leads to a significant resilience to hydrofracture in these regions. Where water drains into crevasses through hillslope flow or smalls streams,

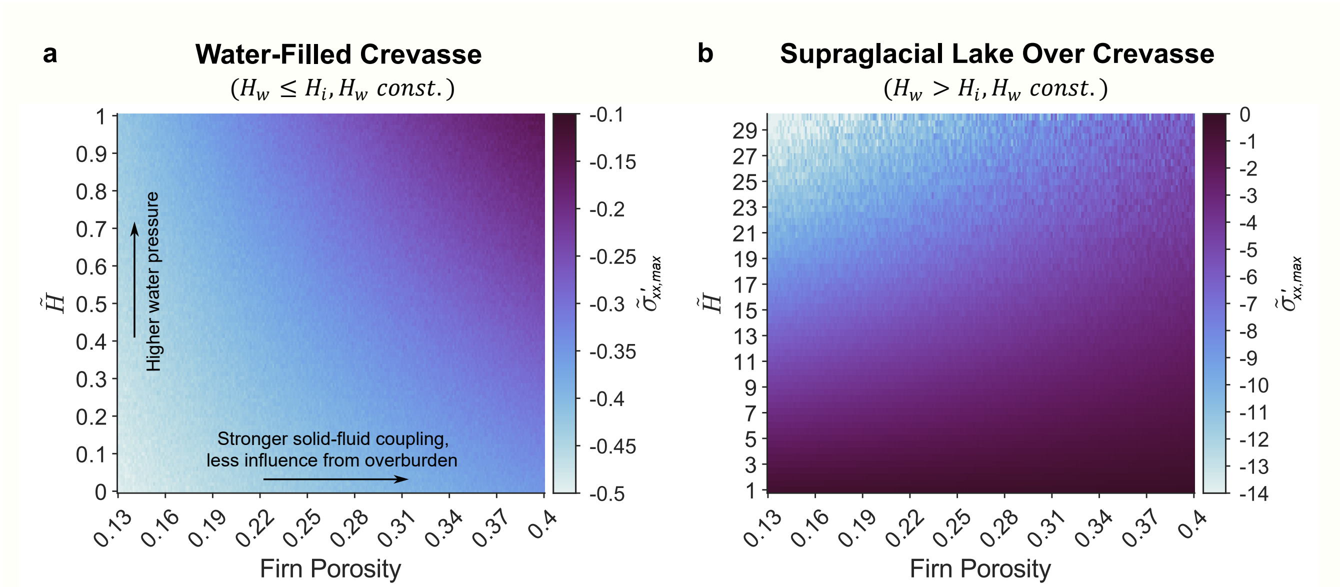

Fig. 11. Non-dimensional maximum effective stress as a function of firn porosity and non-dimensional water height in the crevasse. a) Water-filled crevasses. The non-dimensional effective stress remains compressive but increases a firn porosity increases and water heigh increases due to the increasing water pressure, strong fluid-solid coupling, and reduced lithostatic stress due to a lower Poisson's Ratio. b) Supraglacial lake over a crevasse. Non-dimensional effective stress becomes more compressive as the water level increases, due to the additional lithostatic stress from the overlying lake. Firn porosity plays a great role in determining the non-dimensional effective stress as the water level increases, since it modulates both the hydrostatic stress transmitted to the solid skeleton, and the portion of the lithostatic stress transmitted horizontally.

the rate of water injection into the crevasse is closely balanced by the rate at which water infiltrates into the permeable firn layer. As a result, water will not rise within the fracture and the hydrostatic pressure on the firn remains low and insuffient to cause hydrofracture in the firn layer. Where large streams, rivers, or lakes that intersect fractures, the rate of surface water inflow may be significantly greater than the firn infiltration rate, leading to crevasse filling. However, even in this case, the firn largely stabilizes the system and prevents hydrofracture.

Specifically, we find that at water levels below the critical transition point defined in Eqn, 43, the underlying firn layer experiences a slightly greater maximum effective stress than if the system consisted of solid ice (Figure 10). However, in both cases, the effective stress remains compressive. Once the water level exceeds this transition point, the firn becomes a stabilizing mechanism that significantly reduces the maximum effective stress (Figure 10) as a large portion of the total stress is accommodated by a change in pore pressure, rather than being transmitted to the solid skeleton. In the case of a supraglacial lake, a firn layer is particular stabilizing as the lithostatic stress increases more quickly with lake depth than the hydrostatic stress. Therefore, even in the case of a water-filled crevasse, hydrofracture of a porous firn layer appears to be highly unlikely.

5.1 Implications for Greenland

These results are consistent with the observations of ice blob formation and supraglacial lake drainage in Greenland's ice slab regions discussed in the introduction. Where a porous firn layer exists, the system is infiltration-dominated and leak-off of water from the fracture into the porous firn significantly reduces the likelihood of further crevasse propagation. This process traps liquid water in the upper 2% of the ice column and allows buried regions of saturated firn to form that refreeze over time into ice blobs (Culberg and others, 2022). However, the formation of an ice blob creates a locally solid ice column and subsequent fracture and melt events can lead to classic hydrofracture events, since there is no longer any pore space into which water can leak-off. More generally, this supports the hypothesis of Culberg and others (2022) that a solid ice column is needed for hydrofracture and that therefore, as Greenland warms, there will be a time lag between the development of ice slabs and the formation of surface to bed connections that can couple the supraglacial and subglacial hydrology.

5.2 Implications for Antarctica

These results also have important implications for the future stability of Antarctica's ice shelves. Hydrofracture has been implicated in the breakup of the Larsen B and other ice shelves (Scambos and others, 2000; Banwell and others, 2013; Scambos and others, 2003), leading to a loss of buttressing and significant accelerations in the inland ice flow that increase mass loss from the continent (Scambos and others, 2004; Rignot and others, 2004). However, most ice shelves still retain some firn layer (Alley and others, 2018; Munneke and others, 2014) and previous work hypothesized that all pore space in the firn would need to be filled with refrozen meltwater before hydrofracture could occur. This hypothesis was based on the assumption that surface ponds could not form until the firn layer was completely removed (Munneke and others, 2014).

The discovery of ice slabs in Greenland has since demonstrated that supraglacial hydrology may develop without complete filling of firn pore space (MacFerrin and others, 2019; Tedstone and Machguth, 2022), suggesting a potential mode for more rapid destabilization of ice shelves under ongoing atmospheric warming. Our results now quantitatively demonstrate that even if ice shelves were to develop ice slabs and rapidly transition from firn storage to supraglacial runoff in a similar way to Greenland, this alone would not be sufficient to prime them for immediate hydrofracture-induced disintegration. Instead, complete filling off all local firn pore space is in fact necessary because of the firn's resilience to hydrofracture. This would require a longer period of sustained warming to achieve than the formation of ice slabs alone.

5.3 Assumptions and Future Work

While we have derived a idealized description of maximum effective tensile stress in the firn under a static water load, our results rest on a number of modeling assumptions that should be tested in future work. For example, since capillary pressure is insufficient to drive firn deformation or fracturing, we have focused on water infiltration rates that are much larger than the firn hydraulic conductivity, and thus can safely neglect capillarity in the model. Therefore our model cannot capture the gravity fingering instability under unsaturated flow conditions (Cueto-Felgueroso and Juanes, 2009). The effect of capillarity is beyond the scope of current study, but might be important for studying the formation of ice pipe or ice lens. With large water infiltration rates in the model, it takes only several minutes to penetrate the depth of the firn layer. Therefore we neglect meltwater refreezing that takes hours (Moure and others, 2022) and snow compaction that takes years (Meyer and Hewitt, 2017). In the model, we also assume that the firn layer underneath the crevasse tip is fully permeable and leaves the skeleton stress-free. To span the transition from porous and permeable firn to non-porous and impermeable solid ice, we could introduce a "permeability load parameter" to modulate the boundary condition, as suggested in Auton and MacMinn (2019).

In terms of fracture dynamics, our model only predicts the conditions needed for fracture initiation in the firn layer and does not consider the dynamics of fracture propagation. Future work might consider the behavior of deeper crevasses that partially penetrate the firn layer, or the full transient propagation path of a shallower water-filled crevasse that initially is entirely within the ice slab.

Similarly, here we have considered a static water load, but a fully transient model could be used to study the effect of diurnal fluctuations in water levels (or other transient filling processes) on the evolution of effective stress within the firn layer.

6. Conclusions

Understanding the vulnerability of Greenland's ice slab regions to hydrofracture is critical for assessing where and how quickly the supraglacial and subglacial hydrologic systems can become coupled as the equilibrium line retreats inland. Previous observational work has shown that while meltwater frequently drains into fractures in ice slabs, this water appears to largely be trapped in the underlying porous firn layer (Culberg and others, 2022). However, the question remained as to why these water-filled crevasses would not propagate unstably, as expected for water-filled crevasses in solid ice. Here, we developed a poromechanical model to analyze the maximum effective stress in the firn layer beneath a water-filled fracture in an ice slab. Our results show that the firn layer stabilizes the system in two ways. First, for low rates of water flow into a crevasse, this water can quickly leak-off into the firn and prevent the crevasse from filling in the first place. Second, even if water can fill the crevasse, a significant portion of the hydrostatic stress is accommodated by changes in pore pressure, reducing the effective stress felt by the solid skeleton and preventing fracture propagation. However, once all pore space in the firn is filled with refrozen solid ice, this advantage is lost, and full ice thickness hydrofracture may occur, explaining why deep lake drainages have also been observed in ice slab regions. Our model now provides a clear physical mechanism for the apparent stability of relict firn layer, as well as an explanation for the observed transition from firn infiltration to surface-to-bed fracturing.[1]

Notes

1 Y. Meng and R. Culberg contributed equally to this work. Y. Meng developed the poromechanical model and conducted the scaling analyses, R. Culberg conceived the study and applied the model to the Greenland ice sheet, and C.-Y. Lai contributed to the development of the analyses and the interpretation of results. All authors contributed to the writing of the paper.

Acknowledgement

Y.M. acknowledges funding from the Cooperative Institute for Modeling the Earth System (CIMES) at Princeton University. R.C. thanks the Department of Geosciences at Princeton University for funding through the Hess Postdoctoral Fellowship. C.-Y.L. acknowledges funding from NSF's Office of Polar Programs through OPP-2235051.

Appendix

Convergence and mesh independence analysis

Figure 12 shows the time evolution of infiltration-induced horizontal effective stress change at the crevasse tip ($\delta\sigma'_{xx,\max}(t)$) under constant pressure and injection velocity conditions. The mesh size decreases from 1 m (900 elements in the domain) to 0.3 m (10000 elements in the domain). The modeling results converge at a mesh size of 0.5 m, which is adopted for all the simulation presented in this paper.

Scaling between $\delta\sigma'_{xx,max}$ and δp under large V_{inj} or L_{crev}

For constant injection velocity cases with an unrealistically large crevasse opening or water injection velocity at the crevasse tip, the invading front keeps expanding in a quarter-circular shape, and H_0 in Eqn. (35) is replaced by the water depth when

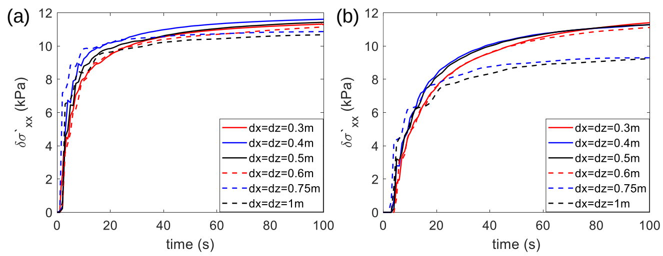

Fig. 12. Convergence and mesh independence analysis. Time evolution of the infiltration-induced horizontal effective stress change at the crevasse tip $\delta\sigma'_{xx}(t)$ for (a) $H_w = 10$ m, (b) $V_{\text{inj}} = 0.05$ m/s, with a decreasing mesh size from 1 m (900 elements in the domain) to 0.3 m (10000 elements in the domain). The modeling results converge at a mesh size of 0.5 m, which is adopted for all the simulation presented in this paper.

we terminate the simulation. We incorporate this scenario into the expression of δp as follows:

$$\delta p = \begin{cases} \frac{2}{\pi}\frac{\eta_w V_{\text{inj}} L_{\text{crev}}}{k_0} ln(\frac{2}{\pi\rho_w g z_0}\frac{\eta_w V_{\text{inj}} L_{\text{crev}}}{k_0}), \text{ if } & V(\alpha H) \leq V_{\text{grav}}, \\ \frac{2}{\pi}\frac{\eta_w V_{\text{inj}} L_{\text{crev}}}{k_0} ln(\frac{\alpha H}{z_0}), \text{ if } & V(\alpha H) > V_{\text{grav}}. \end{cases} \quad (44)$$

where αH is the depth at which we terminate the simulation, and $\alpha = 0.5$ in this paper. The constant injection velocity simulation results for a range of b, V_{inj}, L_{crev}, k_0 (unrealistically large V_{inj} or L_{crev}) agrees well with our proposed scaling $\delta\sigma'_{xx,\max} = 0.22(b\delta p)$ and the analytical expression for δp (Eqn. 44), as shown in Figure 13. This agreement serves as an additional validation of our numerical simulation, and demonstrates the universality of the scaling relationship $\delta\sigma'_{xx,\max} = 0.22(b\delta p)$.

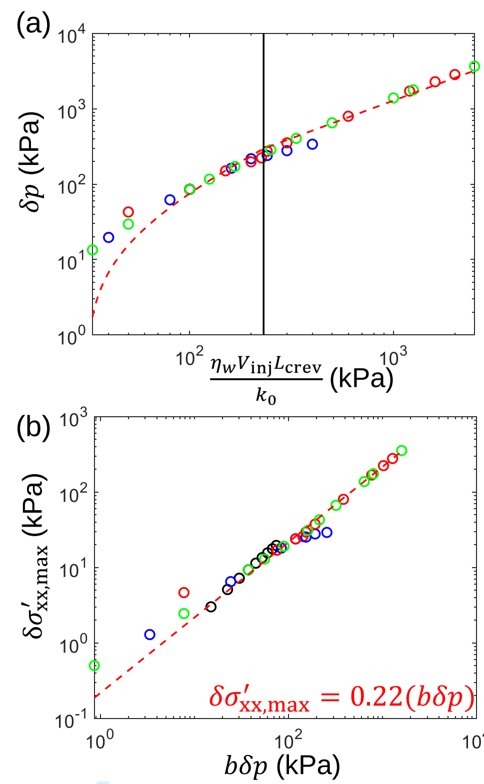

Fig. 13. (a) The scaling between the infiltration-induced pore pressure change at the crevasse tip (δp) and viscous pressure ($\frac{\eta_w V_{\text{inj}} L_{\text{crev}}}{k_0}$) from the water infiltration with a constant injection velocity. The markers represent simulation results as follows: black markers represent cases with $b \in [0, 1]$, blue markers represent cases with $V_{\text{inj}} \in [0.02, 0.2]$ m/s, red markers represent cases with $L_{\text{crev}} \in [1, 10]$ m, and green markers represent cases with $k_0 \in [10^{-10}, 3 \times 10^{-9}]$ m^2. The dashed red line represents analytical prediction from Eqn. (44). (b) The scaling between $\delta\sigma'_{\text{xx,max}}$ and $b\delta p$. Markers represent all simulation data from water infiltration with a constant injection velocity. The dashed red line represents the analytical prediction: $\delta\sigma'_{\text{xx,max}} = \beta\delta p$ (Eqn. (32)), with the prefactor $\beta = 0.22$.

References

Adolph AC and Albert MR (2014) Gas diffusivity and permeability through the firn column at Summit, Greenland: Measurements and comparison to microstructural properties. *Cryosphere*, **8**(1), 319–328, ISSN 19940424 (doi: 10.5194/tc-8-319-2014)

Alley K, Scambos T, Miller J, Long D and MacFerrin M (2018) Quantifying vulnerability of antarctic ice shelves to hydrofracture using microwave scattering properties. *Remote sensing of environment*, **210**, 297–306

Andrews LC, Hoffman MJ, Neumann TA, Catania GA, Lüthi MP, Hawley RL, Schild KM, Ryser C and Morriss BF (2018) Seasonal evolution of the subglacial hydrologic system modified by supraglacial lake drainage in western greenland. *Journal of Geophysical Research: Earth Surface*, **123**(6), 1479–1496

Auton LC and MacMinn CW (2019) Large poroelasto-plastic deformations due to radially outward fluid injection. *Journal of the Mechanics and Physics of Solids*, **132**, 103690

Banwell AF, MacAyeal DR and Sergienko OV (2013) Breakup of the Larsen B Ice Shelf triggered by chain reaction drainage of supraglacial lakes. *Geophysical Research Letters*, **40**(22), 5872–5876, ISSN 00948276 (doi: 10.1002/2013GL057694)

Biot MA (1941) General theory of three-dimensional consolidation. *Journal of applied physics*, **12**(2), 155–164

Bjørnarå TI, Nordbotten JM and Park J (2016) Vertically integrated models for coupled two-phase flow and geomechanics in porous media. *Water Resour. Res.*, **52**, 1398–1417

Brooks RH (1965) *Hydraulic properties of porous media*. Colorado State University

Bunger AP, Detournay E and Garagash DI (2005) Toughness-dominated hydraulic fracture with leak-off. *International journal of fracture*, **134**, 175–190

Chen B, Barboza BR, Sun Y, Bai J, Thomas HR, Dutko M, Cottrell M and Li C (2021) A Review of Hydraulic Fracturing Simulation. *Archives of Computational Methods in Engineering*, **29**(4), 2113–2170, ISSN 18861784 (doi: 10.1007/s11831-021-09653-z)

Christoffersen P, Bougamont M, Hubbard A, Doyle SH, Grigsby S and Pettersson R (2018) Cascading lake drainage on the Greenland Ice Sheet triggered by tensile shock and fracture. *Nature Communications*, **9**(1), 1–12, ISSN 20411723 (doi: 10.1038/s41467-018-03420-8)

Colosio P, Tedesco M, Ranzi R and Fettweis X (2021) Surface melting over the Greenland ice sheet derived from enhanced resolution passive microwave brightness temperatures (1979-2019). *Cryosphere*, **15**(6), 2623–2646, ISSN 19940424 (doi: 10.5194/tc-15-2623-2021)

Coussy O (2004) *Poromechanics*. John Wiley and Sons, Chichester, England

Cueto-Felgueroso L and Juanes R (2009) A phase field model of unsaturated flow. *Water resources research*, **45**(10)

Culberg R, Chu W and Schroeder DM (2022) Shallow Fracture Buffers High Elevation Runoff in Northwest Greenland. *Geophysical Research Letters*, **49**(23), ISSN 19448007 (doi: 10.1029/2022GL101151)

Das SB, Joughin I, Behn MD, Howat IM, King MA, Lizarralde D and Bhatia MP (2008) Fracture Propagation to the Base of the Greenland Ice Sheet During Supraglacial Lake Drainage. *Science*, **320**(May), 778–782

Detournay E (2016) Mechanics of hydraulic fractures. *Annual review of fluid mechanics*, **48**, 311–339

Dow CF, Kulessa B, Rutt I, Tsai V, Pimentel S, Doyle S, Van As D, Lindbäck K, Pettersson R, Jones G and others (2015) Modeling of subglacial hydrological development following rapid supraglacial lake drainage. *Journal of Geophysical Research: Earth Surface*, **120**(6), 1127–1147

Engelder T, Lacazette A, Barton N and Stephansson O (1990) Natural hydraulic fracturing. In *Proceedings of the International Symposium on Rock Joints, 4-6 June at Loen, Norway*, 35–43

Fettweis X, Tedesco M, Van Den Broeke M and Ettema J (2011) Melting trends over the Greenland ice sheet (1958-2009) from spaceborne microwave data and regional climate models. *The Cryosphere*, **5**(2), 359–375, ISSN 19940416 (doi: 10.5194/tc-5-359-2011)

Forster RR, Box JE, Van Den Broeke MR, Miège C, Burgess EW, Van Angelen JH, Lenaerts JT, Koenig LS, Paden J, Lewis C, Gogineni SP, Leuschen C, McConnell JR, Miege C, Burgess EW, Van Angelen JH, Lenaerts JT, Koenig LS, Paden J, Lewis C, Gogineni SP, Leuschen C and McConnell JR (2014) Extensive liquid meltwater storage in firn within the Greenland ice sheet. *Nature Geoscience*, **7**(2), 95–98, ISSN 17520894 (doi: 10.1038/ngeo2043)

Gleason CJ, Smith LC, Chu VW, Legleiter CJ, Pitcher LH, Overstreet BT, Rennermalm AK, Forster RR and Yang K (2016) Characterizing supraglacial meltwater channel hydraulics on the Greenland Ice Sheet from in situ observations. *Earth Surface Processes and Landforms*, **41**(14), 2111–2122, ISSN 10969837 (doi: 10.1002/esp.3977)

Harper J, Humphrey N, Pfeffer WT, Brown J and Fettweis X (2012) Greenland ice-sheet contribution to sea-level rise buffered by meltwater storage in firn. *Nature*, **491**(7423), 240–243, ISSN 00280836 (doi: 10.1038/nature11566)

Hoffman MJ, Perego M, Andrews LC, Price SF, Neumann TA, Johnson JV, Catania G and Lüthi MP (2018) Widespread moulin formation during supraglacial lake drainages in greenland. *Geophysical Research Letters*, **45**(2), 778–788

Jha B and Juanes R (2014) Coupled multiphase flow and poromechanics: A computational model of pore pressure effects on fault slip and earthquake triggering. *Water Resour. Res.*, **50**, 3776–3808

King EC and Jarvis EP (2007) Use of shear waves to measure poisson's ratio in polar firn. *Journal of Environmental and Engineering Geophysics*, **12**(1), 15–21, ISSN 10831363 (doi: 10.2113/JEEG12.1.15)

Koziol C, Arnold N, Pope A and Colgan W (2017) Quantifying supraglacial meltwater pathways in the Paakitsoq region, West Greenland. *Journal of Glaciology*, **63**(239), 464–476, ISSN 00221430 (doi: 10.1017/jog.2017.5)

Lai CY, Kingslake J, Wearing MG, Chen PHC, Gentine P, Li H, Spergel JJ and van Wessem JM (2020) Vulnerability of Antarctica's ice shelves to meltwater-driven fracture. *Nature*, **584**(7822), 574–578, ISSN 14764687 (doi: 10.1038/s41586-020-2627-8)

Lai CY, Stevens LA, Chase DL, Creyts TT, Behn MD, Das SB and Stone HA (2021) Hydraulic transmissivity inferred from ice-sheet relaxation following greenland supraglacial lake drainages. *Nature communications*, **12**(1), 3955

Lewis RW and Schrefler BA (1998) *The finite element method in the static and dynamic deformation and consolidation of porous media*. John Wiley & Sons

MacFerrin MJ, Machguth H, van As D, Charalampidis C, Stevens CM, Heilig A, Vandecrux B, Langen PL, Mottram RH, Fettweis X, van den Broeke MR, Pfeffer WT, Moussavi MS, Abdalati W, van As D, Charalampidis C, Stevens CM, Heilig A, Vandecrux B, Langen PL, Mottram RH, Fettweis X, den Broeke MR, Pfeffer WT, Moussavi MS, Abdalati W, van As D, Charalampidis C, Stevens CM, Heilig A, Vandecrux B, Langen PL, Mottram RH, Fettweis X, van den Broeke MR, Pfeffer WT, Moussavi MS and Abdalati W (2019) Rapid expansion of Greenland's low-permeability ice slabs. *Nature*, **573**(7774), 403–407, ISSN 14764687 (doi: 10.1038/s41586-019-1550-3)

Macferrin MJ, Stevens CM, Vandecrux B, Waddington ED and Abdalati W (2022) The Greenland Firn Compaction Verification and Reconnaissance (FirnCover) dataset, 2013-2019. *Earth System Science Data*, **14**(2), 955–971, ISSN 18663516 (doi: 10.5194/essd-14-955-2022)

Machguth H, Macferrin M, Van As D, Box JE, Charalampidis C, Colgan W, Fausto RS, Meijer HA, Mosley-Thompson E and Van De Wal RS (2016) Greenland meltwater storage in firn limited by near-surface ice formation. *Nature Climate Change*, **6**(4), 390–393, ISSN 17586798 (doi: 10.1038/nclimate2899)

Meng Y, Primkulov BK, Yang Z, Kwok CY and Juanes R (2020) Jamming transition and emergence of fracturing in wet granular media. *Physical Review Research*, **2**(2), 022012

Meng Y, Li W and Juanes R (2022) Fracturing in wet granular media illuminated by photoporomechanics. *Physical Review Applied*, **18**(6), 064081

Meyer CR and Hewitt IJ (2017) A continuum model for meltwater flow through compacting snow. *The Cryosphere*, **11**(6), 2799–2813

Moon T, Joughin I, Smith B, Van Den Broeke MR, Van De Berg WJ, Noël B and Usher M (2014) Distinct patterns of seasonal Greenland glacier velocity. *Geophysical Research Letters*, **41**(20), 7209–7216, ISSN 19448007 (doi: 10.1002/2014GL061836)

Mouginot J, Rignot E, Bjørk AA, van den Broeke M, Millan R, Morlighem M, Noël B, Scheuchl B and Wood M (2019) Forty-six years of Greenland Ice Sheet mass balance from 1972 to 2018. *Proceedings of the National Academy of Sciences of the United States of America*, **116**(19), 9239–9244, ISSN 10916490 (doi: 10.1073/pnas.1904242116)

Moure A, Jones ND, Pawlak J, Meyer CR and Fu X (2022) A thermodynamic nonequilibrium model for preferential infiltration and refreezing of melt in snow. *ESS Open Archive*

Munneke PK, Ligtenberg SR, Van Den Broeke MR and Vaughan DG (2014) Firn air depletion as a precursor of antarctic ice-shelf collapse. *Journal of Glaciology*, **60**(220), 205–214

Poinar K and Andrews LC (2021) Challenges in predicting greenland supraglacial lake drainages at the regional scale. *The Cryosphere*, **15**(3), 1455–1483

Poinar K, Joughin I, Das SB, Behn MD, Lenaerts JT and Van Den Broeke MR (2015) Limits to future expansion of surface-melt-enhanced ice flow into the interior of western Greenland. *Geophysical Research Letters*, **42**(6), 1800–1807, ISSN 19448007 (doi: 10.1002/2015GL063192)

Poinar K, Joughin I, Lilien D, Brucker L, Kehrl L and Nowicki S (2017) Drainage of southeast greenland firn aquifer water through crevasses to the bed. *Frontiers in Earth Science*, **5**, 5

Rignot E, Casassa G, Gogineni P, Krabill W, Rivera A and Thomas R (2004) Accelerated ice discharge from the Antarctic Peninsula following the collapse of Larsen B ice shelf. *Geophysical Research Letters*, **31**(18), 2–5, ISSN 00948276 (doi: 10.1029/2004GL020697)

Sayers CM (2021) Porosity dependence of elastic moduli of snow and firn. *Journal of Glaciology*, **67**(265), 788–796, ISSN 00221430 (doi: 10.1017/jog.2021.25)

Scambos T, Hulbe C and Fahnestock M (2003) Climate-induced ice shelf disintegration in the antarctic peninsula. *Antarctic Peninsula climate variability: Historical and paleoenvironmental perspectives*, **79**, 79–92

Scambos TA, Hulbe C, Fahnestock M and Bohlander J (2000) The link between climate warming and break-up of ice shelves in the antarctic peninsula. *Journal of Glaciology*, **46**(154), 516–530

Scambos TA, Bohlander J, Shuman CA and Skvarca P (2004) Glacier acceleration and thinning after ice shelf collapse in the larsen b embayment, antarctica. *Geophysical Research Letters*, **31**(18)

Schlegel R, Diez A, Löwe H, Mayer C, Lambrecht A, Freitag J, Miller H, Hofstede C and Eisen O (2019) Comparison of elastic moduli from seismic diving-wave and ice-core microstructure analysis in Antarctic polar firn. *Annals of Glaciology*, **60**(79), 220–230, ISSN 02603055 (doi: 10.1017/aog.2019.10)

Schoof C (2010) Ice-sheet acceleration driven by melt supply variability. *Nature*, 6–9, ISSN 0028-0836 (doi: 10.1038/nature09618)

Smith JL (1965) The Elastic Constants, Strength, and Density of Greenland Snow as Determined from Measurements of Sonic Wave Velocity. Technical Report November, CRREL

Smith LC, Chu VW, Yang K, Gleason CJ, Pitcher LH, Rennermalm AK, Legleiter CJ, Behar AE, Overstreet BT, Moustafa SE, Tedesco M, Forster RR, LeWinter AL, Finnegan DC, Sheng Y and Balog J (2015) Efficient meltwater drainage through supraglacial streams and rivers on the southwest Greenland ice sheet. *Proceedings of the National Academy of Sciences of the United States of America*, **112**(4), 1001–1006, ISSN 10916490 (doi: 10.1073/pnas.1413024112)

Stevens LA, Behn MD, McGuire JJ, Das SB, Joughin I, Herring T, Shean DE and King MA (2015) Greenland supraglacial lake drainages triggered by hydrologically induced basal slip. *Nature*, **522**(7554), 73–76

Tedstone AJ and Machguth H (2022) Increasing surface runoff from Greenland's firn areas. *Nature Climate Change*, **12**(July), 672–676, ISSN 17586798 (doi: 10.1038/s41558-022-01371-z)

Terzaghi K (1925) *Erdbaumechanik auf Bodenphysikalischer Grundlage*. F. Deuticke

Terzaghi K (1943) *Theoretical Soil Mechanics*. John Wiley & Sons, Ltd, ISBN 9780470172766

Van Den Broeke M, Bamber J, Ettema J, Rignot E, Schrama E, Van Berg WJD, Van Meijgaard E, Velicogna I and Wouters B (2009) Partitioning recent Greenland mass loss. *Science*, **326**(5955), 984–986, ISSN 0036-8075 (doi: 10.1126/science.1178176)

Van Der Veen CJ (1998) Fracture mechanics approach to penetration of surface crevasses on glaciers. *Cold Regions Science and Technology*, **27**(1), 31–47, ISSN 0165232X (doi: 10.1016/S0165-232X(97)00022-0)

van der Veen CJ (2007) Fracture propagation as means of rapidly transferring surface meltwater to the base of glaciers. *Geophysical Research Letters*, **34**(1), 1–5, ISSN 00948276 (doi: 10.1029/2006GL028385)

Wang HF (2000) *Theory of Linear Poroelasticity*. Princeton University Press

Yang K and Smith LC (2016) Internally drained catchments dominate supraglacial hydrology of the southwest Greenland Ice Sheet. *Journal of Geophysical Research: Earth Surface*, **121**, 1891–1910 (doi: 10.1002/2016JF003927)

Zwally HJ, Abdalati W, Herring T, Larson K, Saba J and Steffen K (2002) Surface Melt – Induced Acceleration of Greenland Ice-Sheet Flow. *Science*, **297**(July), 218–223